# MSc (Physics) Project Course PC5286

# Noise Characterization and Filtering for Co-propagating QKD

by

Zhang Shunyang (A0296417U)

This Project is supervised by Professor Christian Kurtsiefer

and Mr. Peh Yu Xiang, Justin

# Contents

# Chapter 1

# Introduction

## 1.1 Co-propagating Quantum Key Distribution

Quantum key distribution (QKD) has become a mature communication technology[1], providing unconditional security[2] for data transmission based on physical principles rather than purely mathematical assumptions.

Conventionally, most QKD architectures have relied on isolated dark fibers to avoid interference from a classical data link. Although these methods ensure high fidelity, they are impractical for real-world deployments due to the cost of updating facilities. Therefore, investigating how quantum and classical signals can coexist within the same physical medium has become a central essential in applied quantum communication.

As shown in Figure 1.1, traditional QKD requires one bidirectional logical classical channel and one logical quantum channel. However, these channels need not correspond to separate physical ones. By transmitting classical information in the C-band ($\sim$ 1550 nm) and quantum signals in the O-band ($\sim$ 1310 nm), where fiber-related signal attenuation is minimized, a co-propagating protocol can be established, enabling QKD deployment over existing optical infrastructure designed for classical communication.

Continuous-variable quantum key distribution (CVQKD) has been shown to provide a method for establishing a secure quantum connection in co-propagating architectures. In such schemes, the quantum channel encodes information in the continuous states of light, like intensity. When classical and quantum signals share the same physical channel, CVQKD benefits from conventional modulation and detection techniques using stan-

dard telecom components, such as coarse wavelength division multiplexers (CWDM). Recent research has achieved 100 km and 120 km[3] co-propagating connections.

Moreover, CVQKD in a co-propagating regime is easier to deploy than discrete-variable QKD (DVQKD). One reason is that CVQKD offers a higher signal-to-noise ratio due to its higher field intensity, allowing it to tolerate higher co-existing classical optical power. Whereas DVQKD relies on extremely weak single-photon-level pulses and detectors that are very sensitive to stray photons or Raman background noise from classical channels, this results in reduced robustness.

Though CVQKD offers practical advantages in co-propagating cases, it remains inferior to DVQKD in protocol design[4]. Many highly optimized schemes developed for discrete-variable systems, such as entanglement-based and measurement-device-independent protocols, rely on single-photon detection and cannot be directly implemented in CVQKD. These form the reason why co-propagating DVQKD remains a topic worth discussing and examining.

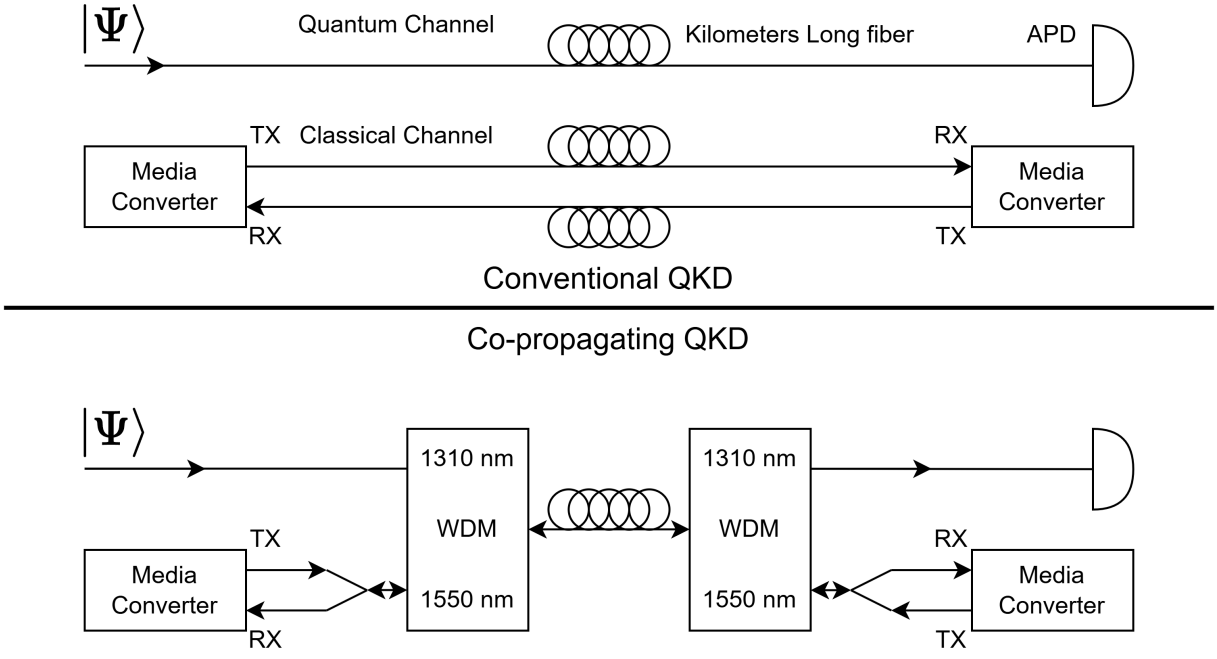


Figure 1.1: Comparing conventional and co-propagation-based QKD. The quantum state $|\Psi\rangle$ represents states used for QKD. The TX and RX labels indicate the transmitting and receiving ports of the classical media converters. WDM represents the Wavelength Division Multiplexer.

According to Figure 1.1, the proposed co-propagating QKD architec-

ture primarily relies on a wavelength-division multiplexer (WDM), which partitions light into different output ports based on their wavelengths. At the same time, the transmitting and receiving ports are designed to share the same optical fiber bidirectionally via an optical circulator.

## 1.2 Issues for Co-propagating

One significant challenge in implementing this architecture is the power difference between classical and quantum signals. The optical power emitted by a laser source in a media converter is typically on the order of milliwatts ($10^{-3}$ $Js^{-1}$). At the same time, single photons in the telecoms band have an energy of approximately $10^{-19}$ J. During co-propagation, noise is introduced around the O-band (quantum) wavelength from the C-band (classical). Also, in practical QKD, the fiber length can usually reach tens of kilometers; Raman scattering[5], back reflections, etc., can leak into the quantum channel and are strongly dependent on the fiber length.

Several key noise mechanisms degrade the performance of a DVQKD system in a co-propagating context[6].

- Spontaneous Raman scattering from the classical channels is a dominant impairment: photons generated by this process can spectrally leak into the quantum channel's wavelength band, thus elevating the quantum bit error rate (QBER).

- Cross-channel interference and back reflections from multiplexing and fiber imperfections can directly introduce stray photons into the single-photon detectors of the quantum receiver.

- Four-wave mixing (FWM) and other mixing effects become significant when classical channel powers are high and channel spacing is small, producing photons with new wavelengths near those of quantum links.

The most critical noise source in co-propagating DVQKD is spontaneous Raman scattering, which arises from the inelastic interactions[7] between photons of the classical channel and the vibration modes of the optical fibers. Unlike linear crosstalk and weak FWM, Raman scattering generates broadband noise photons that extend far from the original wavelength

of the classical signal. Consequently, even when tens of nanometers spectrally separate the quantum channel, scattered photons can still reach the detection bandwidth of the single photon detectors used for QKD.

The strength of Raman scattering usually scales approximately linearly with both the classical signal intensity and the propagation length of the fiber. When classical channels operate at several milliwatts of power, the Raman scattering contribution becomes significant after tens of kilometers of co-propagation, a common situation in practical QKD. As a result, Raman scattering can constitute a dominant source of noise in co-propagating DVQKD systems.

Suppose the mentioned noise factors are not carefully filtered and compensated. In that case, the resulting reduction in signal-to-noise ratio (and, correspondingly, an increase in QBER) will depress the key generation rate in QKD. To address these issues, we first investigate methods for accurately measuring a laser diode's emission spectrum.

The spectrometer used in our experiments must satisfy several technical requirements:

- Sub-nanometer spectral resolution, probably better than 0.1 nm
- Wide dynamic range capable of resolving signals from microwatt-level optical power down to approximately $10^6$ photons per second.
- High repeatability to ensure measurement consistency across runs.

After establishing a reliable method for measuring optical spectra over a wide dynamic range, the spectrometer can then serve as a tool for evaluating the performance of the co-propagating systems. It can be used either to verify the filtering quality of optical components, ensuring that most of the noise originating from the classical channel is effectively suppressed, or to quantify how the Raman noise level changes with fiber length. This spectral characterization provides essential feedback for optimizing wavelength division multiplexing configurations, filter design, and overall system stability in practical QKD implementations.

In the following chapters, we will discuss the efforts made to build the spectrometer from both hardware and software perspectives. Additionally, we will examine the need to construct a cascaded grating spectrometer. Lastly, we will address noise factors present in the proposed QKD architec-

ture in both forward and backward directions, along with their respective solutions.

Finally, with a relatively comprehensive understanding of the spectral behavior of noise sources such as Raman scattering and back-reflection, it will be possible to know how the ideal co-propagating QKD architecture described in Figure 1.1 needs to be modified for deployment in production scenarios.

# Chapter 2

# Grating Spectrum Measurement

## 2.1 Diffraction Grating

Reflective diffraction grating mirrors, characterized by their periodically structured reflective surfaces that spatially separate light into distinct diffraction orders [8], can be used to measure the wavelength spectrum of light. The diffraction can be described mathematically by the grating equation

$$d\,(\sin\theta_i + \sin\theta_m) = m\lambda, \tag{2.1}$$

where $\theta_i$ is the incident angle, $\theta_m$ is the diffraction angle of order $m$, $\lambda$ is the wavelength, and $d$ is the period of the grating groove, namely grating spacing. A schematic representation is shown in Figure 2.1

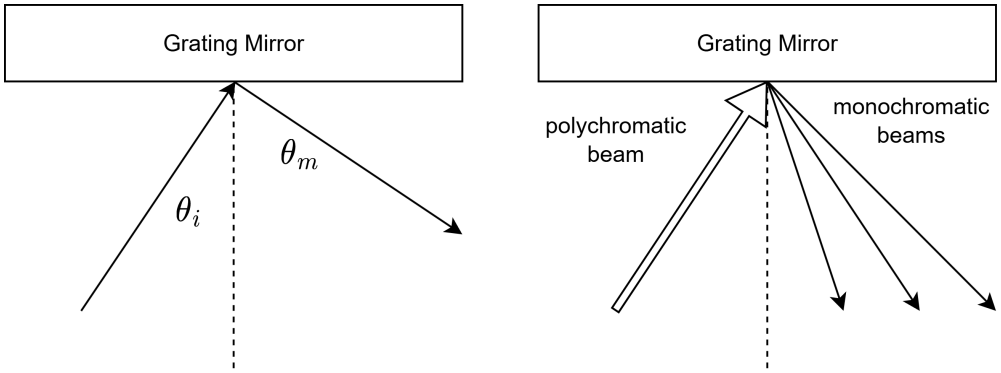


Figure 2.1: Diffraction Grating

Multiple spectrometer designs have been realized by others with distinct

pros and cons; some choose to rotate the mirror, while others prefer to fix the mirror but move the detector[9].

Given the devices available and the difficulties of calibrating and programming, the most suitable method for us would be to rotate the grating mirror and try to couple a free-grating period that must be carefully chosen.

Numerical analysis is essential for selecting components, as inappropriate choices can lead to difficulties with optical alignment and data processing. Starting with the grating mirror, the grating period must be carefully chosen to ensure that the target wavelength range, approximately 1200 nm to 1600 nm, is mapped to a limited angular range, ideally around $10^\circ$ , so that the resolution of 40 nm/$^\circ$ is given.

From the grating equation given, let the wavelength difference be $\Delta\lambda = 1600 - 1200 = 400$ nm. Assuming a normal incident angle ($\theta_i = 0$) and applying the small-angle approximation for simplicity, the variation on the $m = 1$ order of diffraction angle given a period $d$ is expressed by

$$\Delta\theta(d) \approx \frac{\Delta\lambda}{d} \tag{2.2}$$

Based on this conclusion, a grating mirror designed for 1000 nm with a groove density of $600^{-1}$mm (600 grooves per millimeter) was selected for the spectrometer. This configuration yields a total angular dispersion of approximately $13.751^\circ$ across a 400 nm wavelength range, which is close enough to the desired $\sim 10^\circ$ target.

The grating mirrors described above were mounted on a K10CR1 rotary stage. According to the manufacturer's datasheet, the stage exhibits a unidirectional repeatability of 0.1 nm[10] in measured wavelength. Given the angle-wavelength relationship shown in equation 2.2, where $d = 1666.7$ comes from 600 grooves per millimeter, this corresponds to a wavelength uncertainty of 0.1 nm. Consequently, the constructed spectrometer can be expected to achieve a wavelength precision of $\sim 0.1$ nm in the absence of other error sources, which is sufficient for the current stage of the experiment.

The overall schematic of the system is illustrated in Figure 2.2. The detection section is left blank, as multiple measurement methods have been developed and tested, each with its own characteristics, which will be de-

scribed in detail later in this chapter. Before that, the procedures for constructing and calibrating the grating spectrometer are first introduced.

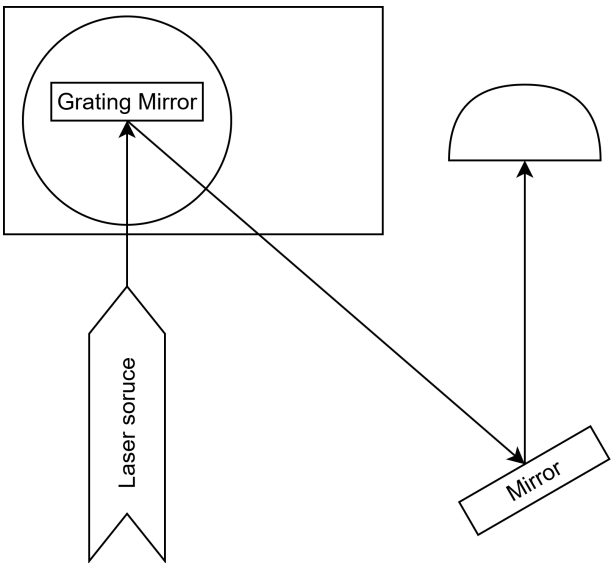


Figure 2.2: Spectrometer Schematic

## 2.2 Build the Spectrometer

Given the measurement architecture, we define the configuration in which the grating mirror grooves are perpendicular to the optical table as the zero-roll, zero-pitch state, thereby simplifying alignment in the vertical direction. When a grating mirror is mounted on the rotary stage, the yaw can be adjusted freely while the non-zero pitch can be canceled by applying an opposite pitch to the plane mirror shown in Figure 2.2. Consequently, the roll (lateral rotation) remains the only degree of freedom that requires fine manual adjustments.

Different from the other two degrees of freedom, the roll of the grating mirror has a pronounced effect on the dependence of the spectrometer's overall transmission efficiency on the angles due to the geometry of the grating. When a beam is incident on the grating mirror at zero pitch, the diffracted monochromatic components propagate in a plane perpendicular to the grating grooves. A non-zero roll angle results in a vertical spatial walk-off for all diffracted beams with a non-zero $\theta_m$ value.

To ensure the $\theta_{\text{roll}}$ is as close to zero as possible, a common practice is to utilize beams corresponding to different diffraction orders $m$. This is

equivalent to selecting two diffracted beams that lie on the plane perpendicular to the groove direction for alignments. The alignment procedures are:

1. Rotate the grating mirror (change its yaw) so that $m = 1$ and $m = -1$ beams diffracted from a monochromatic laser source (usually a 1310nm coherent beam with sub-nanometer line width) are approximately symmetric with respect to the incident beam.

2. Place a cardboard screen along the path of the $m = 1$ beam at a sufficiently long distance (on the order of several meters) to amplify any vertical spatial walk-off. Record the beam position on the screen using an infrared (IR) viewing card and a marking pen.

3. Rotate the grating mirror so that the $m = -1$ diffracted beam reaches the same screen, and mark its position as well.

4. Compare the vertical separation between the two marks. Adjust the grating mirror's roll angle accordingly. Repeat the procedure until the two marks from $m = 1$ and $m = -1$ beams overlap.

Therefore, it can be reasonably assumed that the spatial walk-off resulting from an almost zero roll angle affects transmission efficiency only to a minor extent and in a controlled manner.

With the grating mirror set to approximately zero roll, free-space coupling between the plane mirror and the fiber-optic collimator is established using conventional alignment techniques. Coarse alignment is performed by observing the back-reflected light, followed by fine adjustment using a power meter.

In addition, the scanning process with the constructed spectrometer yields only angle–voltage data pairs, indicating that a mapping between the motor angles and wavelengths should be established. We define $\theta_c$ as the coupling angle, representing the angle between the incident beam and the first-order diffracted beam. Since the alignment beam has a wavelength of 1310 nm, we set $\theta_i = 0$ to correspond to this wavelength. Using equation

2.1, and let $\theta_i = 0$ at 1310 nm calibration wavelength:

$$\lambda(\theta_i) = d\left[\sin\theta_i + \sin(\theta_c - \theta_i)\right] = 2d\,\sin\left(\tfrac{\theta_c}{2}\right)\cos\left(\theta_i - \tfrac{\theta_c}{2}\right). \tag{2.3}$$

$$\lambda(0) = d\sin\theta_c = 1310 \text{ nm}, \tag{2.4}$$

$$\text{thus } \theta_c \approx 51.8^\circ. \tag{2.5}$$

## 2.3 Direct Powermeter Measurements

Using the constructed spectrometer and the mapping, the next step is to determine how to measure the output intensity. One of the most straightforward approaches is to directly connect the collimator output to a power meter (PM). The deployed PM has a wavelength-dependent responsivity characterized precisely between 800 nm to 1800 nm.

The five selectable resistors have resistances of 20 Ω, 1 kΩ, 10 kΩ, 99.1 kΩ, and 1 MΩ. If necessary, a wavelength-dependent index $\alpha(\lambda)$ can be introduced to calculate the power of the laser by

$$P = \frac{V}{R * \alpha(\lambda)},$$

where $R$ is the selected resistance and $V$ is the nominal voltage.

The C-band source used for testing is a 1550 nm distributed Bragg fiber laser diode, driven by a laser controller with a proportional–integral–derivative (PID) temperature control loop. In addition, tuning the diode temperature allows fine adjustment of the emission wavelength, as the diode's structure expands with increasing temperature[11] and contracts with cooling.

The measured spectral density is presented in Figure 2.3, where the y-axis is plotted on a logarithmic scale while the wavelength x-axis is linear. From the plot, it can be concluded that the dynamic range of this measurement method is approximately 30 dB. Although this dynamic range is insufficient for precise scattering measurements due to the upper and lower limit of scattering differing far more than that, additional limitations of the power meter have been identified. These issues can be categorized into high-frequency and low-frequency components.

The high-frequency noise observed in the measurement can be primarily due to thermal noise[12], also known as Johnson noise, or shot noise. This

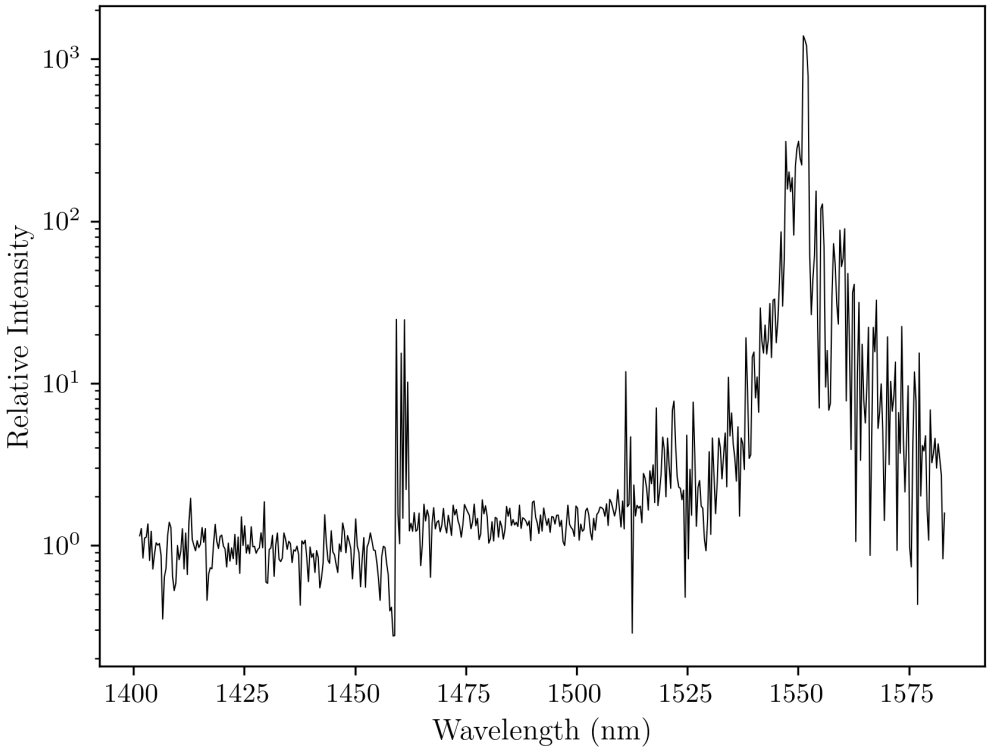


Figure 2.3: The resulting spectral density for the diode laser, when the power meter is used for intensity detection.

type of noise is typically broadband and exhibits weak dependence on the applied voltage, adding up as background noise. The presence of Johnson noise significantly limits the ability to directly measure weak optical signals. When the noise amplitude exceeds the signal level by several orders of magnitude, repeated measurements can improve measurement accuracy. Still, they may not be so helpful when the actual signal strength is too low.

In addition to high-frequency components, low-frequency noise, probably caused by power supply voltage drift or variations in room temperature, and typically at frequencies on the order of mHz, is also a significant concern in most measurements. For instance, a 4001-point scan usually takes six hours. That is long enough for low-frequency noise to affect measurement accuracy significantly.

Mitigating both high- and low-frequency noise through post-processing alone is challenging. Purely script-based filtering methods are insufficient to reduce the noise to an acceptable level. To overcome this limitation, a measurement approach incorporating additional hardware components is introduced in the following section.

## 2.4 Lock-in Amplifier with PM

### 2.4.1 Filtering and Measurement Results

A lock-in amplifier is connected to the PM's analog output to improve signal detection. Lock-in amplifiers are widely used to extract extremely weak signals from noisy environments, provided that the signal frequency differs sufficiently from that of the dominating noise components [13]. This property makes lock-in amplifiers particularly suitable for addressing the limitations encountered in direct power-meter measurements.

To briefly illustrate the operating principle of the lock-in amplifier and mathematically explain how it suppresses noise in our measurement system,

we let the PM output being:

$$S(t) = S_0 + n(t), \tag{2.6}$$

where $S_0$ is the optical signal and $n(t)$ is the noise.

If we modulate the optical signal with a square wave at frequency $f_c$:

$$C(t) = \mathrm{sgn}\big(\sin(2\pi f_c t)\big), \tag{2.7}$$

the modulated detector signal becomes

$$S_{\mathrm{mod}}(t) = S_0\, C(t) + n(t). \tag{2.8}$$

The lock-in amplifier uses a reference signal at the same frequency:

$$R_x(t) = \cos(2\pi f_c t), \qquad R_y(t) = \sin(2\pi f_c t). \tag{2.9}$$

The outputs are obtained by multiplications and low-pass filtering:

$$X(t) = \mathrm{LPF}\{\, S_{\mathrm{mod}}(t)\, R_x(t)\,\}, \qquad Y(t) = \mathrm{LPF}\{\, S_{\mathrm{mod}}(t)\, R_y(t)\,\}. \tag{2.10}$$

Since $S_{\mathrm{mod}}(t)$ contains a component at $f_c$, the low-pass yields

$$X \approx \tfrac{1}{2} S_0, \qquad Y \approx 0. \tag{2.11}$$

The final lock-in output amplitude is

$$A = \sqrt{X^2 + Y^2} \;\approx\; \tfrac{1}{2} S_0. \tag{2.12}$$

In some implementations, phase shifts can occur between the reference and the modulated signals due to delays introduced by optical modulations or electronic amplifications. These effects are not accounted for in the theoretical derivation but can be neglected in practice by taking the Euclidean norm of $X$ and $Y$ as the final output.

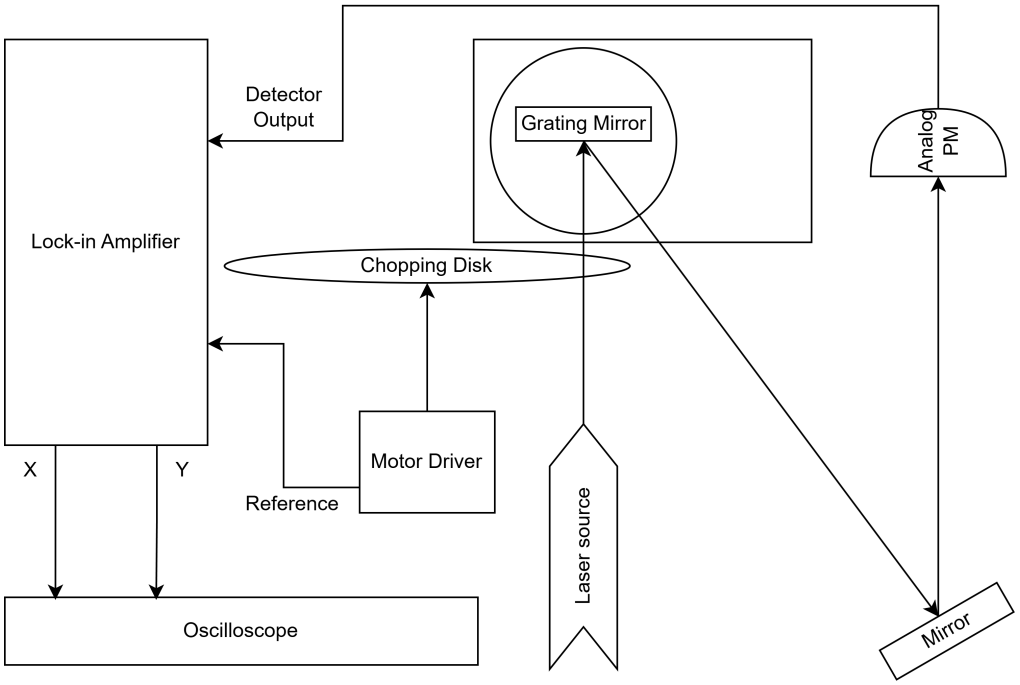


Figure 2.4: Lock-in Amplifier spectrometer.

A chopping disk, illustrated as an ellipse in Figure 2.4, is employed to modulate the optical signal. The disk is positioned between the plane mirror and the collimator, driven by a tunable motor driver. It has 20 evenly spaced openings and occupies half the total arc length when added up. The motor driver simultaneously provides a square-wave reference signal to the lock-in amplifier at a frequency equal to $n$ times the disk's rotational frequency ($n = 20$ in our case). This configuration converts the steady optical output into a periodic signal, which is subsequently detected by the power meter and distinguished from background noise by the lock-in amplifier.

The rotation frequency of the chopping disk is 8.75 RPS(revolution per second) to ensure that the modulation frequency remains within the operational limits of the motor driver. Under these conditions, the chopping frequency, namely the frequency of the square-wave modulation applied to the optical signal, is given by $8.75 * 20 = 175$ Hz.

To acquire the spectrum, the measurement is not based on a single voltage reading, as in a PM with a direct digital output to a computer. The output $X(t)$ and $Y(t)$ are recorded by an oscilloscope over a short time interval to average out fluctuations arising from lock-in amplification instability. The final PM voltage is then obtained by computing the time-

averaged magnitude of these components,

$$V_{\mathrm{PM}} = \langle X(t)^2 + Y(t)^2 \rangle_t$$

After converting the measured voltages to relative optical intensity, the resulting spectrum is plotted in Figure 2.5.

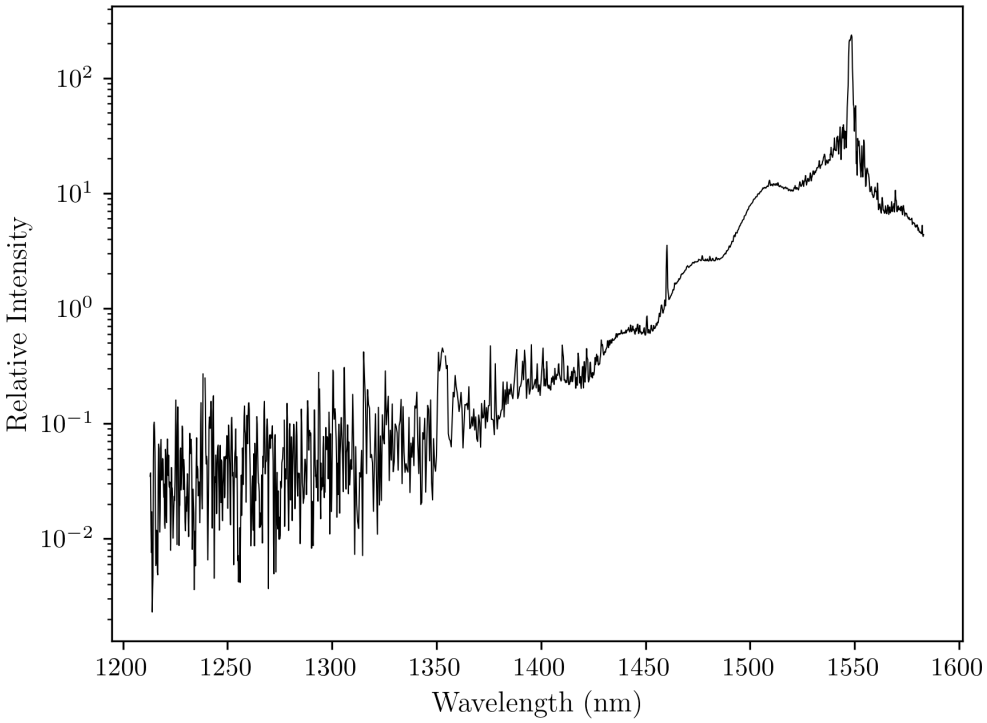


Figure 2.5: Spectral density of the diode laser measured by PM with a lock-in amplifier for noise suppression.

From the plot, the noise level is about $10^{-3}$ of the peak height when it deviates from the C-band center or when the spectral density exhibits a non-monotonic decrease, in other words. Theoretically, the noise originating from the power meter should be effectively suppressed under ideal lock-in detection. These observations, therefore, suggest the presence of additional noise sources that the lock-in amplification process itself may have introduced.

### 2.4.2 Noise Analysis

To further investigate the source of noise, the analysis is extended from the time domain to the frequency domain by performing a Fourier transform on the time-series data. As an illustrative example, a fast Fourier transform

(FFT) was applied to the data recorded at 1310 nm and the resulting plot is provided in Figure 2.6. Peaks can be observed, revealing the presence of periodic components in the noise, likely from the physical or electronic characteristics of the additional components deployed to the system.

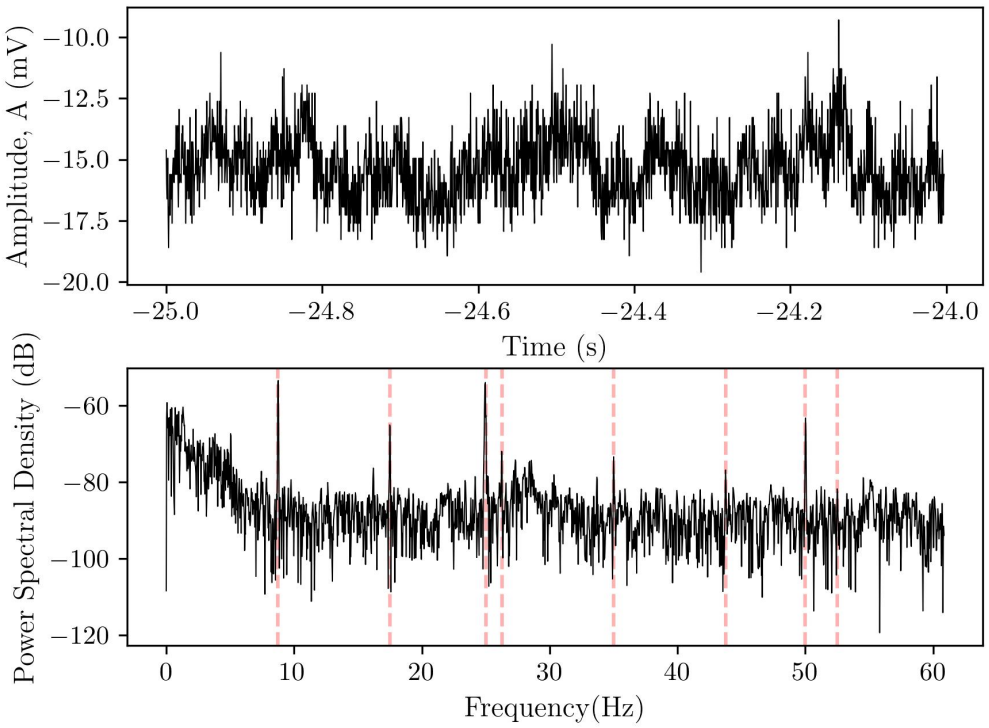


Figure 2.6: Top: Amplitude in the time domain. Bottom: Amplitude in the frequency domain, by performing FFT. Spikes are marked by red dashed lines.

Given that the chopping disk rotates at 8.75 RPS, slight mechanical imbalances are almost inevitable due to imperfect alignment between the disk mass center and its rotational axis. Such an imbalance induces minor vibrations at approximately the same frequency as the disk's rotation, which in turn affects the coupling efficiency between the output beam and the collimator through spatial walk-off. If this effect does exist in the measurement, periodic peaks should appear in the frequency domain at integer multiples of the rotational frequency. That is $8.75n$ Hz, $n \in \mathbb{Z}^+$ (including 8.75, 17.5, 26.25, 35, 43.75, and 52.5). This behavior is indeed observed in the Fourier spectrum, as indicated by the vertical dashed lines in Figure 2.6.

The lock-in amplifier itself is also highly likely to be susceptible to external oscillating signals[14], since the mains power supply connected to it is alternating current (AC) oscillating at 50 Hz. This frequency is clearly

evident in the Fourier spectrum, indicating that the AC power supply partially contributes to the increasing noise level.

The origin of the peak at 25 Hz remains unexplained. It may result from interactions between the alternating current (AC) power supply and specific mechanical or electronic components, effectively producing a subharmonic noise. Alternatively, there can be modulations between the 8.75 Hz motor vibration and the 50 Hz power supply oscillation, $8.75 * a + 50 * b = 25$ for instance. A detailed analysis of this coupling mechanism requires further investigation and is beyond the scope of the present discussion.

In summary, the dynamic range of this method approaches 50 dB. However, the noise level at the order of $10^{-3}$ of the beam emission peak height prevents the reliable detection of photon-level signals. For noise and scattering measurements, it remains essential to achieve a detection threshold of at least $10^6$ photons $s^{-1}$ to offer enough sensitivity.

## 2.5 Tunable Attenuation Avalanche Photon Diode

Avalanche photo diodes (APDs) are widely recognized for their high sensitivity[15] in detecting weak signals. However, due to the intrinsic mechanism of avalanche multiplication, which involves a time cost characterized by the avalanche time constant plus dead-time due to recovery requirements, APDs exhibit a limited count-rate capability, usually around $10^6$ cps(count per second), at a $\sim 1$ % detection efficiency for the InGaAs APDs. Beyond this limit, the avalanche process cannot fully recover between successive photon arrivals, leading to overlapping detection events. This phenomenon, commonly known as saturation, is the main challenge in extending the system's dynamic range.

Moreover, the relationship between count rate (cps) and optical intensity cannot be assumed to be linear[16], as higher photon flux increases the probability of temporal overlap between detection events, leading to multiple photons being counted as a single event. As a result, the count rate must be maintained well below the saturation threshold to ensure accurate measurements.

### 2.5.1 Variable Optical Attenuator

One effective solution is to introduce a variable optical attenuator (VOA) before the APD, allowing the attenuation to be adjusted as needed to reduce the nominal detection efficiency by a known factor when the output beam intensity is high, and increase it when the intensity is low. The VOA used in this experiment is the V1550F from Thorlabs, which internally has a voltage-controlled free-space beam-coupling mechanism based on reflection. Due to the high sensitivity of free-space coupling to alignment, an attenuation exceeding 25 dB can be readily achieved.

Next, a calibration scan was conducted to establish the relationship between the applied voltage and the VOA's actual attenuation. The measurement result, showing the relationship between attenuation and the applied voltage, is shown in Figure2.7.

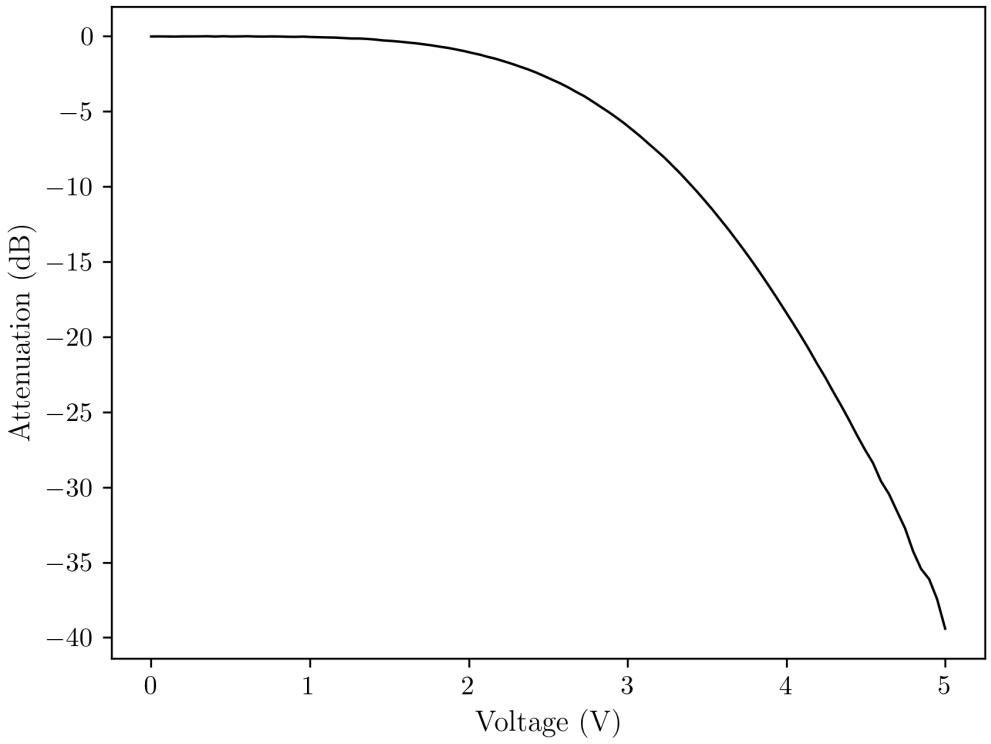


Figure 2.7: Attenuation of the VOA as a function of voltage applied, plotted in log scale.

However, in practical measurements spanning a broadband wavelength range, the VOA may not provide identical attenuation at a fixed control voltage. Using the spectrometer as a selectable wavelength band-pass filter, an attenuation-voltage scan is performed at different wavelengths. The results are presented in Figure2.8. As shown by the color map, the VOA

exhibits significant wavelength dependence at higher voltages, particularly above 4.5 V. This voltage range should therefore be avoided in the following measurements to maintain consistent attenuation performance.

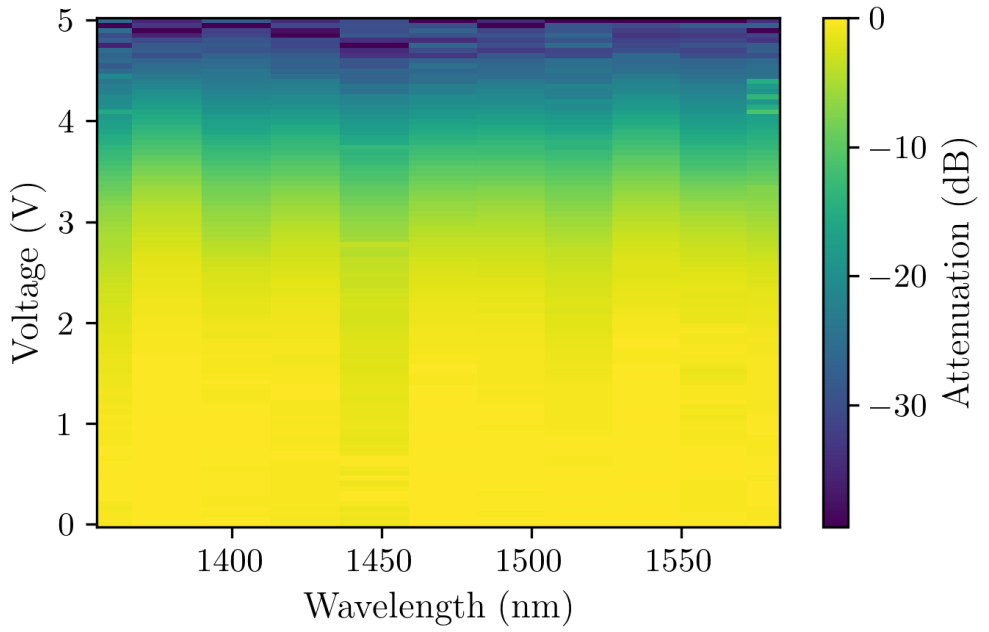


Figure 2.8: The VOA's attenuation as a function of applied voltage and photon wavelength is shown in the plot. The measurement was done with 11 wavelengths and 101 voltage samplings.

### 2.5.2 Measurement Results and Noise Analysis

APDs also exhibit dark counts on the order of $10^4$ cps, similar to PM dark current. These dark counts are mainly shot-noise-limited (time-independent Poisson noise) and are likely due to thermally generated carriers or semiconductor defects. Importantly, because the APD output is time-stamped and processed digitally, these dark counts are largely unaffected by drifting Johnson noise. Other time-dependent noise sources such as background light, inadequate current filtering, or temperature fluctuations can be minimized by maintaining stable environmental conditions during measurements. In summary, most random noise levels can be reduced by increasing the integration time, thereby improving the statistical accuracy of the photon-count estimate.

Following the described method, the measurement results are presented in Figure 2.9. The plot shows that the noise level appears constant on a log scale when the integration time is held steady at one second, suggesting

it depends less on wavelength. Also, the noise can be further reduced by increasing the integration time. The achieved dynamic range is approximately 50 dB, comparable to that of using the PM and lock-in amplifier, while retaining the capability to detect photon-level signals.

In further experiments, optical filtering components will be applied to the original C-band diode laser, resulting in significant attenuation of the spectral density at wavelengths far from the 1550 nm center. Under those circumstances, the combined VOA–APD detection method is the most suitable approach to perform high-precision spectrum measurements.

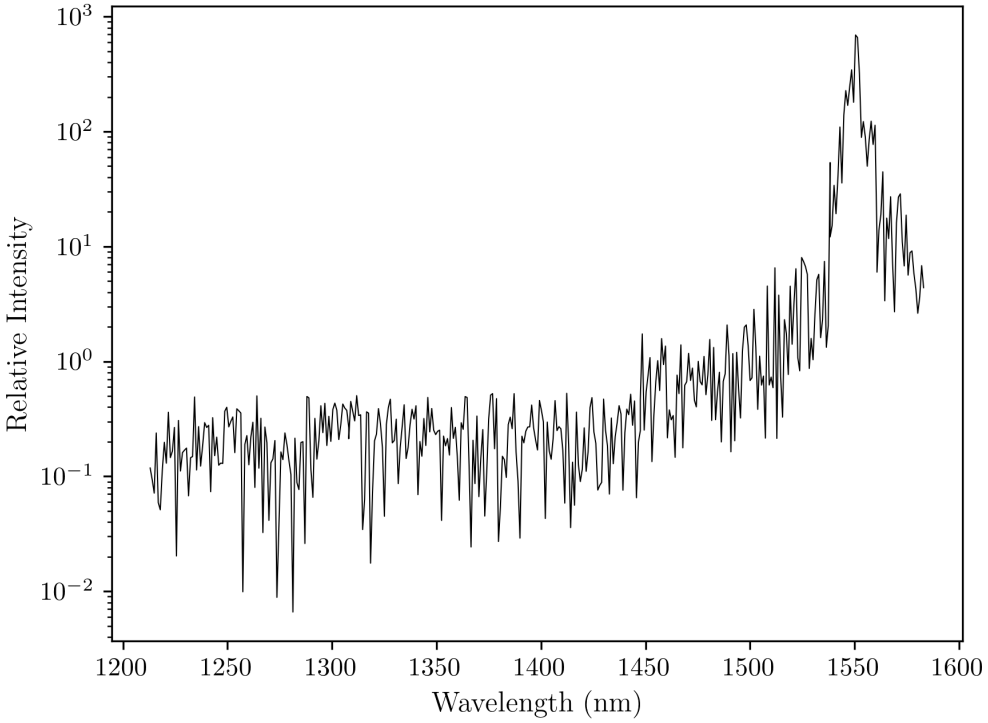


Figure 2.9: Spectral density of the C-band diode laser measured using an APD with controlled attenuation

## 2.6 Direct OSA Measurements and Quantitative Comparisons

An optical spectrum analyzer (OSA) is also introduced for reference measurements. Up to this point, the tests have primarily focused on determining the dynamic range but not the reliability of the spectra obtained. The OSA serves as a benchmark for evaluating the accuracy of the free-space optical spectroscopy system's results.

However, OSA lacks the sensitivity required to detect photon-level signals across most of its operational wavelength range. A test showed that a beam with power half the APD saturation count ($\sim 5 * 10^5$ cps) is indistinguishable from background noise in the OSA, even with the most reasonable integration time and amplification applied, which is the typical intensity range for the scattering we want to characterize.

The measurement results obtained from the OSA, illustrating the spectral density of the C-band diode laser used throughout this work, are presented in Figure 2.10.

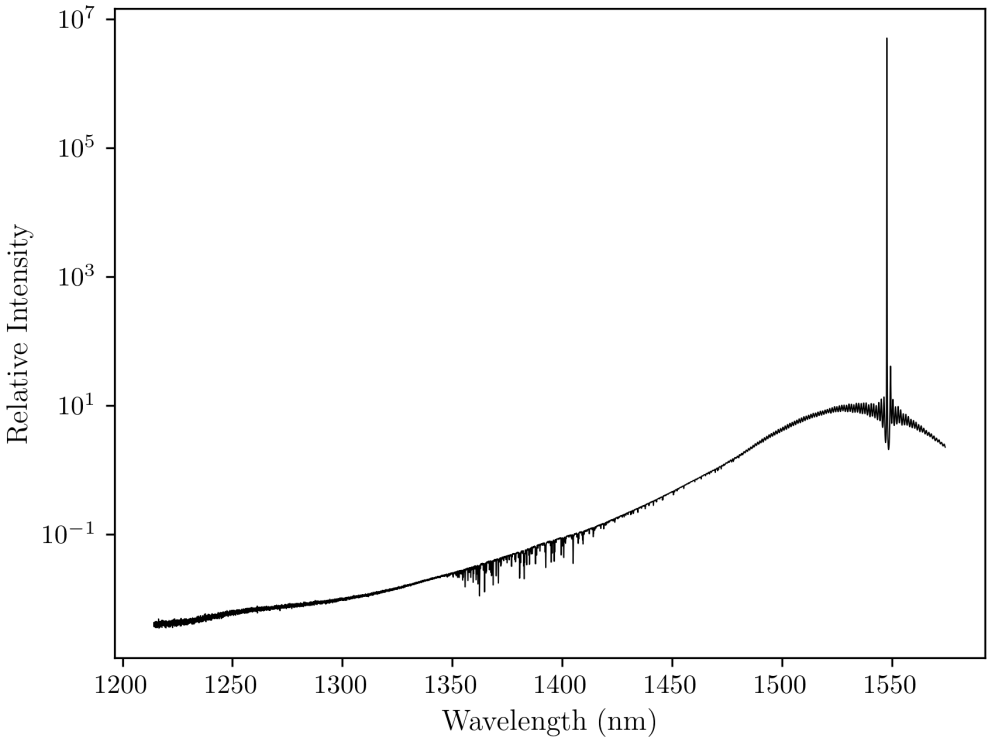


Figure 2.10: Relative spectral density measured by an OSA.

First, by examining a small segment of the spectrum along the wavelength axis, one can observe fine oscillations added to the spectral curve, resembling a high-frequency modulation of the main signal. These features most likely come from reflections between fiber-coupling interfaces or free-space optical surfaces, effectively forming miniature cavities. Similar behaviors also presents in much larger and better optical devices[17] whenever there exist layers of components. Therefore, these oscillations are not expected to form a significant challenge to the overall accuracy of the OSA measurements.

Moreover, a key distinction between the spectra obtained from the OSA and those measured using the grating spectrometer is the relative peak height at the C-band center. Here, the peak height is defined as the intensity difference between the maximum point and the surrounding flat region of the spectrum, which is $\sim$ 60dB for the OSA case and $\sim$ 20dB for others.

To address this discrepancy, it is essential to realize that the output collimator of the spectrometer does not exclusively accept photons of a single wavelength, as would be expected in an ideal configuration [18]. In the perfect case, the collimator instrument response function would resemble a delta distribution. However, both collimators exhibit two-dimensional Gaussian-like response functions in practice.

Practically, the dependence of peak height on the instrument response function's full width half max (FWHM) can be derived as follows:

$$S_{\text{measure}}(\lambda) = (S_{\text{true}} * h)(\lambda), \tag{2.13}$$

$$S_{\text{true}}(\lambda) = H_0\delta(\lambda - \lambda_0) \Rightarrow S_{\text{measure}}(\lambda) = H_0 h(\lambda - \lambda_0), \tag{2.14}$$

$$S_{\text{peak}} = H_0 h(0) = h(0) \quad (H_0 = 1), \tag{2.15}$$

$$h_\Gamma(\lambda) = \frac{1}{\Gamma}\varphi\left(\frac{\lambda}{\Gamma}\right), \quad \int \varphi(u)\, du = 1,\ \Gamma \propto \text{FWHM} \tag{2.16}$$

$$\Rightarrow\ S_{\text{peak}} = \frac{c}{\Gamma} \propto \frac{1}{\text{FWHM}}. \tag{2.17}$$

If we accept that the peak height scales linearly with the inverse of the instrument response function's FWHM, the OSA-to-spectrometer FWHM ratio calculated from peak heights would be on the order of $10^4$, which probably does not make much sense. A more realistic estimate follows from the measured linewidth and normalization:

$$\frac{\text{FWHM}_{\text{spectrometer}}}{\text{FWHM}_{\text{OSA}}} \approx 2.4 \text{ nm}/30 \text{ pm} \approx 80.$$

This latter value is consistent with expectations, i.e., a grating spectrometer FWHM of several nanometers versus an OSA FWHM of 30 picometers.

In most cases, the broad instrument response of our spectrometer is not an issue because our primary interest lies in O-band noise, which exhibits fewer spectral peaks. However, when peak amplitudes must be quantified

accurately, the measured spectra should be deconvolved to recover the true peak heights.

## 2.7 Summary

The spectral densities obtained from different measurement methods can be plotted together in a single figure after appropriate scaling, using the OSA result as the reference baseline. Several observations can be picked up from Figure 2.11 together with the conclusions discussed earlier in this report.

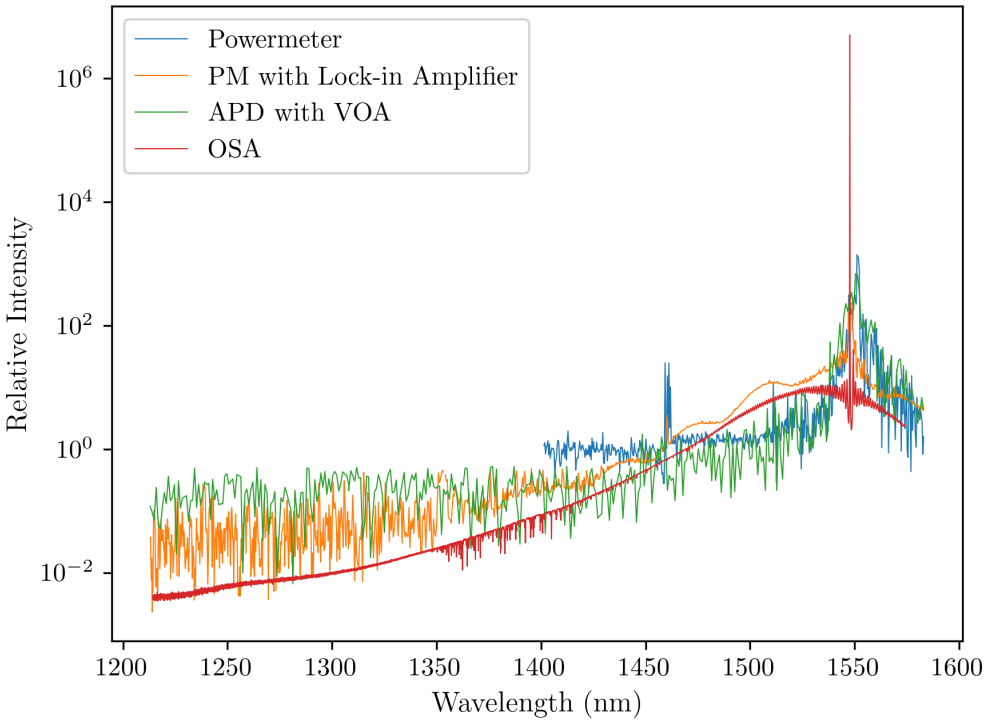


Figure 2.11: A summary of all the methods tried to perform the measurements on a logarithmic scale. The intensity values of each curve was modified for a better visualization.

First, the primary advantage of using a power meter (PM) for intensity measurements lies in its speed. A short integration-time PM requires less than 1 second to transmit the measured beam intensity to the computer, so the dominant time cost during spectral scanning arises from the rotation of the motorized stage holding the grating mirror. However, PM is vulnerable to short- and long-term noise; the former reduces the dynamic range, while the latter cannot be effectively mitigated. Consequently, although the PM is suitable for hardware alignment and calibration procedures, it is not ideal

for applications requiring high sensitivity, such as scattering or filtering characterization.

Second, combining the PM with a lock-in amplifier and periodically modulating the spectrometer output can effectively suppress both high- and low-frequency noise components inherent to the PM, therefore extending the dynamic range to approximately 50 dB. The trade-off is that the lock-in amplifier itself brings noise into this system due to mechanical vibrations, the main electric power supply, and possible nonlinear interactions between them. As a result, photon-level signals at the spectral tails remain either undetectable or require a long integration time.

Despite increasing noise level problems, measurements using a lock-in amplifier require significantly more time than those performed with the power meter alone. This is because the lock-in amplifier provides an analog output that must be recorded over time. Furthermore, after each change of the motor angle, a delay of several seconds is required for the lock-in amplifier to stabilize.

Although the OSA offers excellent accuracy and stability, it is not an ultimate solution for spectral measurements. Its sensitivity to low photon flux is considerably lower than that of the APD, and the OSA cannot meet the sensitivity requirements necessary for our measurements, especially when filters and scatterings are involved.

Finally, spectral measurements in this work primarily rely on the APD combined with a VOA, provided a sufficiently long integration time is used to average out the dark counts. If required, an additional VOA can be cascaded before the APD to extend the dynamic range.

# Chapter 3

# Cascaded Grating Spectrometer

## 3.1 Leakage from Grating Mirror - Potential Solution

However, according to the spectrometer measurements presented in Figure 2.3, Figure 2.5, and Figure 2.9, the relative intensity at the spectral tails near the O-band wavelengths is higher than that measured by the OSA. While this difference can be partially attributed to the broader instrument response function, this factor is insufficient to account for the rising background observed when the scanned wavelength exceeds 100 nm the 1550 nm center.

To verify the nature of that leakage, an optical isolator was placed after the coherent light source to reduce the number of reflected photons entering the laser diode, thereby improving linewidth stability. Additionally, a thick optical cloth was deployed to cover the laser diode and several fiber couplers to suppress ambient light leakage. These do not help reduce the leakage.

One measurement results are presented in Figure 3.1. The spectrum recorded at different temperatures exhibit similar shapes, with a wavelength shift of a few nanometers. This indirectly verifies the wavelengths of the photons reaching the output collimator, as the observation indicates that the tail noise originates in the laser rather than in ambient light. Also, this behavior aligns with the expected thermal expansion of the laser diode structure. From these observations, it can be concluded that the

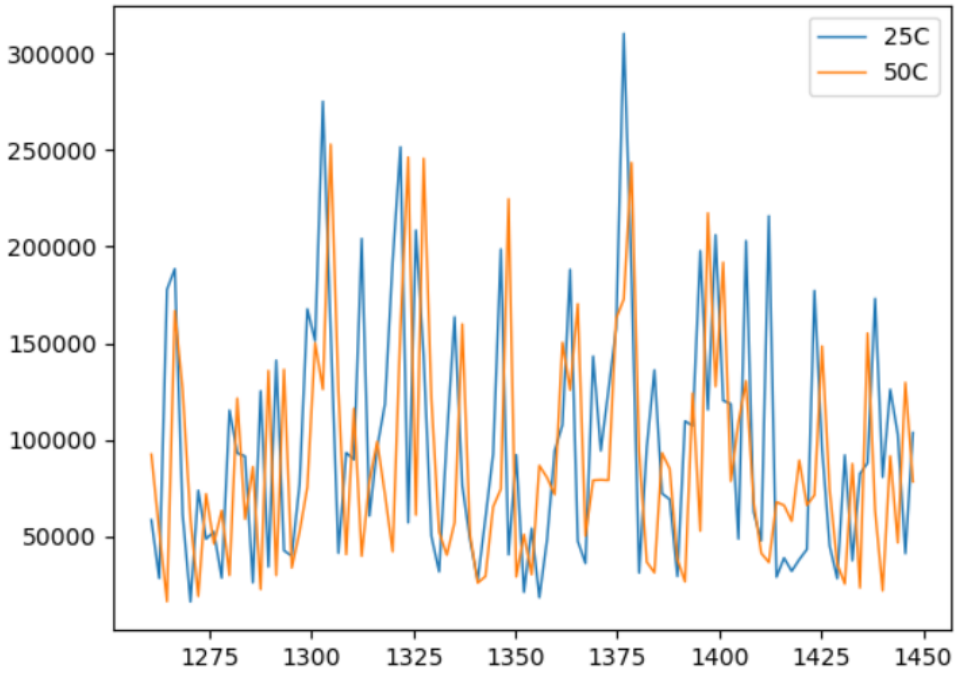


Figure 3.1: APD count vs. Wavelength, vertical-axis is count per second measured by the APD, and horizontal-axis is wavelength in nanometers. The two temperatures selected for this measurement are 50 °C and 25 °C.

high-intensity tail noise primarily comes from leakage through the spectrometer's grating mirror.

We also introduced a long-pass filter RG695. It has an optical density of 3 for photons with wavelengths less than 660 nm and filters out most visible light. The filter was placed at various positions between different components of the spectrometer. According to the similar spectrum measurements as presented in Figure 3.1, the tail spectrum remains almost unchanged, indicating that the noise level does not strongly correspond to stray visible light photons accidentally entering the output collimator.

In conclusion, even when the grating mirror is set to an angle corresponding to wavelengths far from the C-band center (near the O-band region), the measurements still reveal residual leakage from the C-band. This effect is likely caused by imperfections in the diffraction grating itself[19] or by higher-order diffraction components that coincidentally propagate toward the output.

We can consider modeling these imperfections by letting the total mea-

sured intensity at 1310 nm be

$$I_{1310} = I_{\text{real}} + I_{\text{tail}},$$

where the $I_{\text{real}}$ represents the real spectral intensity and $I_{\text{tail}}$ denotes the leakage from the grating mirror. The measurement process using the grating spectrometer can then be described by:

$$I_{\text{real}} + I_{\text{tail}} \overset{\text{spectroscope}}{\longrightarrow} \gamma * (I_{\text{real}} + I_{\text{tail}} * \eta), \tag{3.1}$$

where $\gamma$ is the overall transmission efficiency of the spectrometer, and $\eta$ is the leakage coefficient.

If the conclusion above is valid, one solution is to construct a cascaded grating spectrometer by adding an additional grating mirror. The measurement model can then be expressed as:

$$I_{\text{real}} + I_{\text{tail}} \overset{\text{spectroscope}}{\longrightarrow} \gamma\gamma_{\text{grating}} * (I_{\text{real}} + I_{\text{tail}} * \eta^2), \tag{3.2}$$

with $\gamma_{grating}$ being the efficiency of that extra grating mirror. Since $\eta << 1$, cascading two gratings results in the leakage term being proportional to $\eta^2$, therefore reducing $I_{\text{tail}}$ by a significant amount. Finally, the contribution of $I_{\text{real}}$ becomes increasingly dominant in the measured signal, reducing the data's sensitivity to grating leakage.

## 3.2 Build the Cascaded Spectrometer

Upgrading from a single-grating to a cascaded configuration requires modifications to the structural design, alignment procedure, and angle-wavelength mapping.

Starting from the configuration illustrated in Figure 3.2, the two grating mirrors are arranged in centrally symmetric positions, with an additional mirror pair to compensate non-zero pitch errors. This modification helps reduce alignment complexity and improves overall optical stability.

The free-space alignment procedure, unlike that of the single-grating one, consists of three main components: grating mirror–collimator coupling, diffracted beam–mirror coupling, and forward–backward light cou-

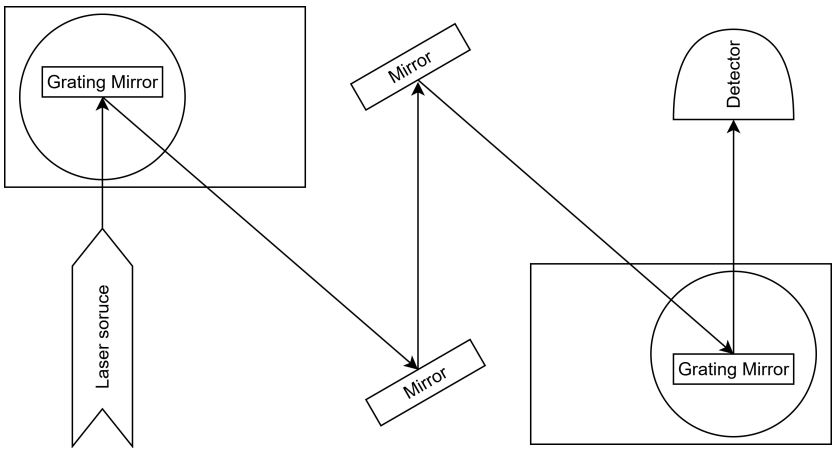


Figure 3.2: Cascading grating spectroscope

pling.

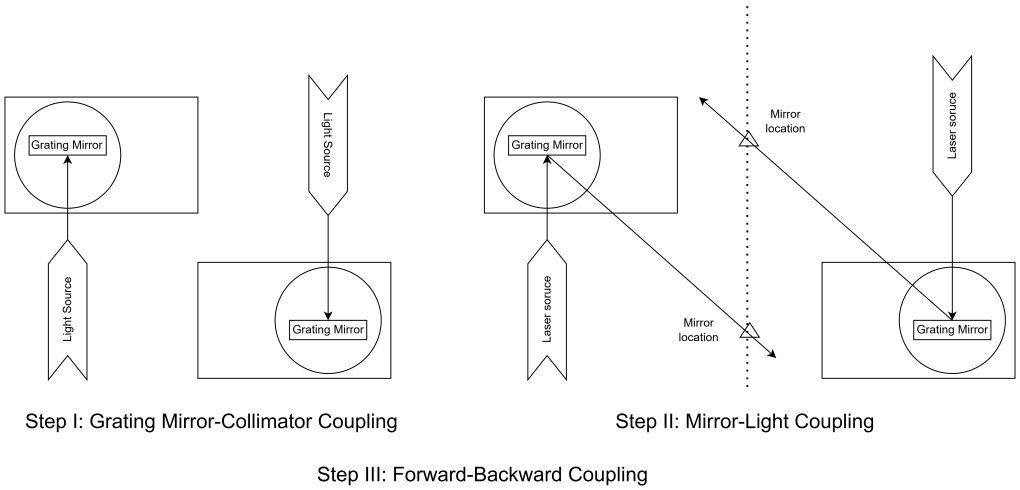


Figure 3.3: Steps for cascading spectrometer calibration, refer fig3.2 for step III.

The first step is to ensure that the incident directions of the collimators are aligned with the normal of the diffraction surface of the grating mirror. Under this condition, the zeroth-order diffracted light returns to the fiber connected to the collimator, providing a stable reference for assessing whether further alignment is required.

However, since infrared (IR) viewing cards are the primary tools available for visualizing telecom wavelength light and are insufficiently sensitive to detect the weak light leaking from fibers, visible light is preferred for the collimator–mirror alignment process. An additional advantage of using visible light in this setup is that the collimators employed in the cascaded grating spectrometer are standard reflective types that use parabolic mirrors rather than lenses to couple the free-space beam into the fiber, thereby

avoiding chromatic aberration in lenses used with a polychromatic beam. This reflective design minimizes wavelength dependence, allowing nearly identical behavior across different wavelengths[20].

Accordingly, the single-mode fiber (SMF) attached to the collimator is temporarily replaced with a red-light ($\sim$ 600 nm) SMF, whose end is connected to a visible laser source bright enough to be observed by the naked eye.

SMF consists of a concentric core surrounded by cladding. When the reflected photons are significantly misaligned from the fiber core, no noticeable effect occurs. However, if the photons strike the cladding instead, imperfect propagation within the fiber causes strong scattering, leading to visible light leaking through the fiber buffer and jacket, observable to the naked eye. As alignment improves and the reflected beam couples more effectively into the fiber core, the scattering intensity decreases.

Based on this phenomenon, the alignment procedure is performed as follows:

1. Adjust the grating mirror yaw by adjusting the motor angle while tuning the collimator pitch. Stop when visible light leaks from the fiber.

2. Fine-tune the grating mirror pitch to locate the minimum scattering intensity (the "valley") between two peaks of leakage brightness.

3. Perturb motor angle and repeat previous step to try minimizing the valley intensity.

4. Terminate when the minimum leakage is achieved, indicating optimal red-light coupling between the mirror and fiber.

At this stage, the mirror normal can be considered approximately aligned with the collimator incident beam direction.

To achieve reliable beam–mirror coupling, a 1310 nm coherent beam is transmitted through the two collimators so that grating diffraction occurs again. The first-order diffracted beam is then observed from a top-down perspective to trace its propagation path. A reference optical axis is defined to pass through the center of the central symmetry and to be approximately parallel to the incident beams from collimators. The two intersection points

between the diffracted-beam trajectories and this reference optical axis are the optimal positions for the two mirrors to reflect the beam.

We perform beam overlapping for forward–backward coupling. A beam splitter divides the original beam and sends it to collimators. Only the two plane mirrors are adjusted. An IR viewing card is placed between the mirrors for simultaneous observation.

With the three coarse couplings, we remove the beam splitter and finalize the fine alignment by carefully adjusting the plane mirrors to optimize beam coupling to maximize transmission through the system.

## 3.3 Calculate Wavelength from Motor Angles

We need a new mapping function from motor angle to measured wavelength—a Littrow-like estimation[21] can be used to simplify the derivations. The two motor angles $\phi_1$ and $\phi_2$ are assumed to be equal, where each angle is defined relative to the yaw position corresponding to the mirror–collimator coupling alignment. Under this approximation, the wavelength–angle relationship can be expressed as:

$$\lambda_\phi = 2 * d * \sin(\theta_{1310} + \phi),\ d = 1/600 \text{ mm}. \tag{3.3}$$

Here, $\theta_{1310}$ represents the coupling angle. In non-ideal conditions, perfect central symmetry cannot be achieved because the incident directions of the two collimators may not be strictly parallel, and no mechanical constraint ensures that the two plane mirrors are perfectly symmetric. These imperfections can be modeled as beam deflections along the propagation path.

For mathematical simplicity, this deflection is treated as a single bending event occurring midway between the two gratings. A two-dimensional ray-tracing algorithm is then employed to determine the motor angles corresponding to photons of different wavelengths that reach the detector under various nonzero $\kappa$ values, where $\kappa$ denotes the beam-bending angle. The solutions are obtained using a bisection method.

The results of the numerical simulations are shown in Figure 3.4. Even under the most extreme conditions, $\kappa = 20°$the simulated curve shifts only

slightly away from that of the perfectly aligned case. This indicates that deviations from central symmetry have a negligible effect on the mapping function between motor angles and wavelength.

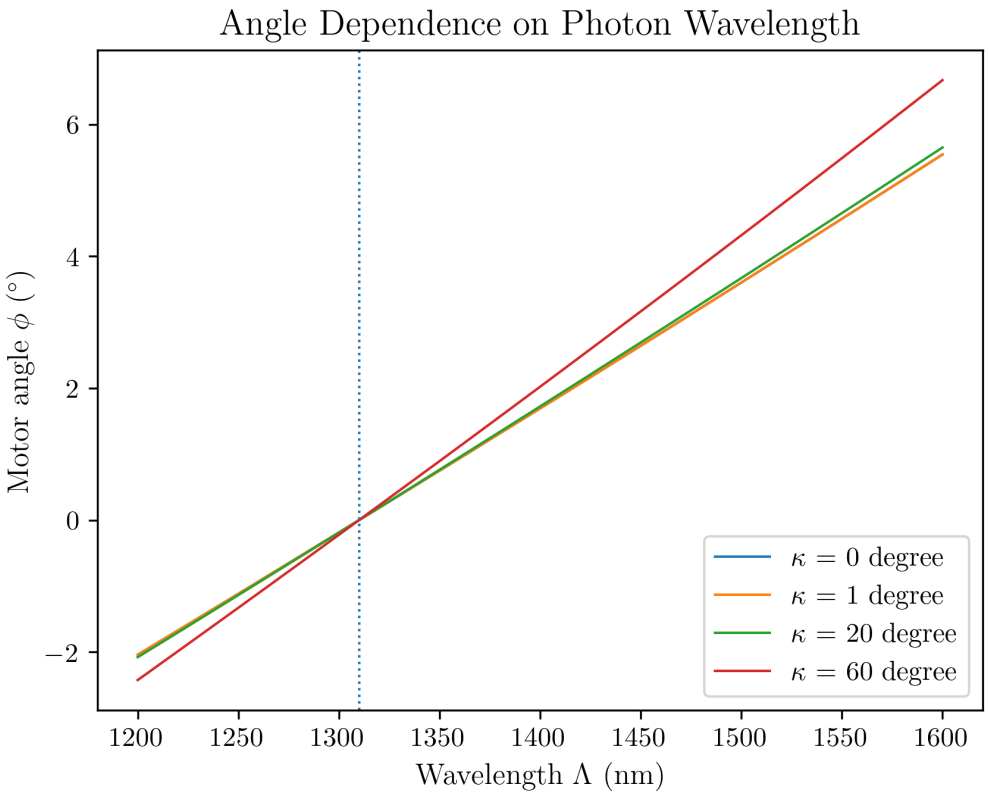


Figure 3.4: Numerically solved relationships between motor angle $\phi$ and wavelength needed for a photon to reach the detector, with or without a bent diagonal ray.

## 3.4 2-D Convolution and Response Function

In this section, we quantitatively examine the spectrometer's resolution characteristics. In a single-grating spectrometer, the spatial walk-off of diffracted beams is angular; thus, increasing the free-space propagation length after the grating can enhance spectral resolution.

We begin with a quantitative analysis of the angle-wavelength mapping functions. The relationship is given:

$$\lambda(\theta_i) = 2d \sin\left(\tfrac{\theta_c}{2}\right) \cos\left(\theta_i - \tfrac{\theta_c}{2}\right)$$

for the single grating case and

$$\lambda_\phi = 2 * d * \sin(\theta_{1310} + \phi)$$

for the cascaded grating case. Given $\theta_c \approx 51.8°$,$\theta_{1310}$ can be derived by

$$\theta_{1310} = \sin^{-1}(\frac{1310 * 10^{-9}}{2 * \frac{10^{-3}}{600}}) \approx 0.403 \text{ rad} = 23.141°. \tag{3.4}$$

With the constants fixed, we differentiate both mapping functions with respect to their motor angles to obtain the wavelength–angle sensitivities near the O-band and small motor rotations:

$$\frac{d\lambda(\theta_i)}{d\theta_i} = d*\sin(\theta_i + 64.1°)*\cos\left(\frac{\theta_i}{2}\right)+2*d*\cos(\theta_i + 64.1°)*\sin\left(\frac{\theta_i}{2}\right) \tag{3.5}$$

and

$$\frac{d\lambda_\phi}{d\phi} = 2 * d * \cos(\phi + 23.141°). \tag{3.6}$$

Within the approximate angle range we measure from $-2°$ to $6°$, the cascaded-grating spectrometer demonstrates much higher wavelength sensitivity to changes in motor angle. Consequently, the cascaded-grating spectrometer provides a lower angular resolution than the single-grating system when the free-space propagation lengths are identical.

Rather than increasing the angular separation of polychromatic photons, an alternative approach is to optimize the collimators' response functions. The IRF of each collimator can be modeled as an isotropic Gaussian function, with any blocked region assigned a value of 0.

With the collimator position fixed and the beam translating along the x-axis through the collimator aperture:

$$\text{IRF}_{\text{collimator}} = \text{IRF}(x, y, \sigma, d) \tag{3.7}$$

$$:= \mathcal{N}_{norm} \exp\left(\frac{-(x - x_0)^2 - y^2}{2\sigma^2}\right)\mathbf{H}(x - d), \quad \mathbf{H} = \begin{cases} 0, & x < d \\ 1, & x \geq d \end{cases}. \tag{3.8}$$

Here, $\mathcal{N}_{norm}$ is a normalization constant, and $\mathbf{H}$ is a unit step function representing the blocking effect of the blade. Meanwhile, the beam translated

along the x-axis can be described by:

$$\mathrm{A}(x, y, \sigma, s) := A_0 \exp\left(\frac{-(x - s - x_0)^2 - y^2}{2\sigma^2}\right), \tag{3.9}$$

$A_0$ is the intensity coefficient and $s$ represents the position of the beam on the x-axis. The overall non-normalized instrument response function $\mathrm{IRF}_{\mathrm{tot}}(s)$ can be obtained by performing a spatial integral of $\mathrm{IRF}(x, y, \sigma, d)\mathrm{A}(x, y, \sigma, s)$:

$$\mathrm{IRF}_{\mathrm{tot}}(d) = \iint_S \mathrm{IRF}(x, y, \sigma, d)\mathrm{A}(x, y, \sigma, s)\, dx\, dy \tag{3.10}$$

$$= \mathcal{N}_{norm} A_0 \int_{y=-\infty}^{\infty} \int_{x=d}^{\infty} \exp\left(\frac{-(x - s - x_0)^2 - (x - x_0)^2 - 2y^2}{2\sigma^2}\right) dx\, dy \tag{3.11}$$

$$= \mathcal{N}_{norm} A_0 \sigma\sqrt{\pi} \int_{x=d}^{\infty} \exp\left(\frac{-(x - s - x_0)^2 - (x - x_0)^2}{2\sigma^2}\right) dx \tag{3.12}$$

$$\text{let } x_0 = 0 \text{ temporarily,} \tag{3.13}$$

$$\mathrm{IRF}_{\mathrm{tot}}(d) = \mathcal{N}_{norm} A_0 \sigma\sqrt{\pi} \int_{x=d}^{\infty} \exp\left(\frac{-2(x - \frac{s}{2})^2 - \frac{s^2}{2}}{2\sigma^2}\right) dx \tag{3.14}$$

$$= \mathcal{N}_{norm} A_0 \sigma\sqrt{\pi} \exp\left(\frac{-s^2}{4\sigma^2}\right) \int_{x=d}^{\infty} \exp\left(\frac{-(x - \frac{s}{2})^2}{2\sigma^2}\right) dx, \tag{3.15}$$

$$\text{by bringing } x_0 \text{ back,} \tag{3.16}$$

$$= \mathcal{N}_{norm} A_0 \frac{\sigma^2\pi}{2} \exp\left(\frac{-s^2}{4\sigma^2}\right) \mathrm{erfc}(\frac{d - x_0 - \frac{s}{2}}{\sigma}), \tag{3.17}$$

with $\mathrm{erfc}(x) = \frac{2}{\sqrt{\pi}} \int_x^{\infty} e^{-t^2}\, dt$ denotes the complementary error function. By evaluating $\mathrm{IRF}_{\mathrm{tot}}(s)$ as a functional of $d$, we can see by how much the FWHM of the instrument response can be reduced and what the cost of transmission efficiency we need to pay as a trade-off is.

We perform an experiment to verify the setup: a blade held vertically by a movable clamp adjusts from partially to fully blocking the output collimator. The spectral density of a coherent beam at each blade position will be measured to fit the spectral peak position and amplitude as functions of blade position.

The comparison in Figure 3.5 shows close agreement between simulated and experimental results, indicating that the model reliably predicts how blade blocking affects the collimator IRF.

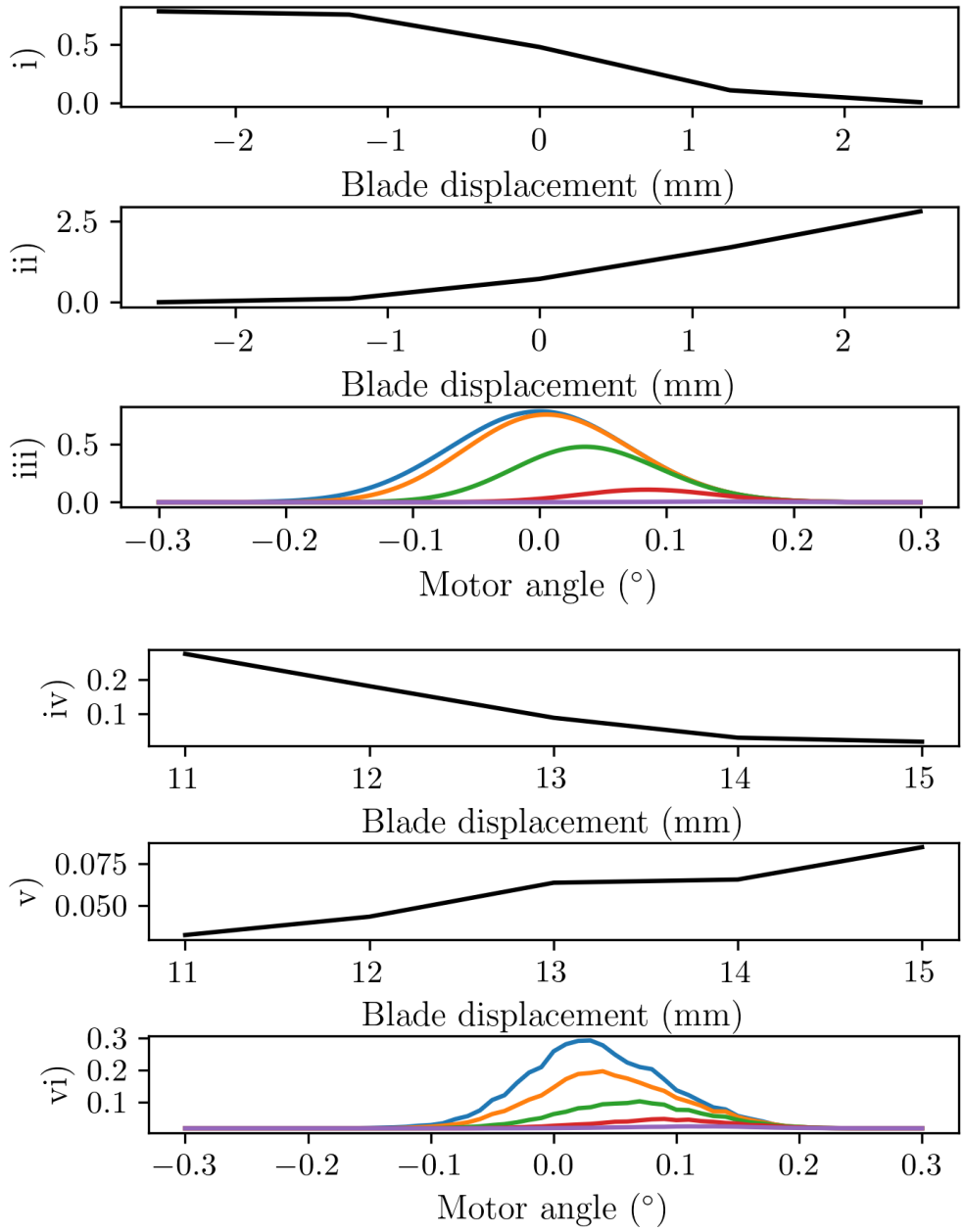


Figure 3.5: i) and iv): Spectral densities for different blade displacements and corresponding fitted or measured Gaussian wave packets for the expected and measured cases. ii) and iii), v) and vi): Fitted or measured Gaussian amplitude and mean (peak center) vs. blade displacement for expected and measured cases.

Consider adding a tunable-radius iris concentric with the output collimator to reduce the IRF FWHM. The FWHM and iris size relationship can be modeled by examining the IRF of the collimator without the iris and the incoming Gaussian beam:

$$\mathrm{IRF}_{\mathrm{iris}}(x,y) = \mathcal{N} e^{-\frac{x^2+y^2}{2\sigma^2}}, \quad A(x,y,s) = A_0 e^{-\frac{(x-s)^2+y^2}{2\sigma^2}}, \tag{3.18}$$

By adding an iris, the overall IRF of the system output is

$$\mathrm{IRF}_{\mathrm{tot}}(r) = \iint_{x^2+y^2\le r^2} \mathrm{IRF}_{\mathrm{iris}}(x,y)\, A(x,y;s)\, dx\, dy \tag{3.19}$$

$$= \mathcal{N} A_0\, e^{-s^2/(4\sigma^2)} \iint_{x^2+y^2\le r^2} e^{-\frac{(x-\frac{s}{2})^2+y^2}{\sigma^2}}\, dx\, dy. \tag{3.20}$$

Numerical evaluation of the aperture-limited model shows that the system response FWHM approaches $\sqrt{2}\sigma$ when $r \to \infty$ and $\sigma$ when $r \to 0$. Thus, even with an infinitesimally small iris[22], the maximal FWHM reduction is limited to a factor of $\sqrt{2}$ with a trade-off of zero transmission.

Consequently, further enhancement must rely on post-processing approaches such as deconvolution during data analysis. However, these methods are inherently limited by the presence of noise that cannot be entirely suppressed.

## 3.5 Wavelength Dependence of Transmission

It is also necessary to characterize the wavelength dependence of the transmission efficiency, since all previous conclusions regarding convolution effects, blade blocking, etc., were derived under the assumption that the incident photons have a wavelength of 1310 nm and that the motor angles are fixed at $\phi_1 = \phi_2 = 0°$.

The transmission efficiency can be considered constant across motor angles only under a two-dimensional approximation. In three dimensions, it is impossible to guarantee that the rolls of the diffraction gratings are perfectly zero: nonzero motor angles introduce vertical spatial walk-off. Furthermore, since plane mirrors necessarily have a nonzero pitch to compensate for the height difference between the two collimators, their reflective performance in beam-fiber couplings cannot be assumed to remain

identical across all motor angles.

To address this, we introduce a tunable laser (TSL) capable of sending beams with wavelengths ranging from 1260 nm to 1360 nm at adjustable intensities. The TSL serves as a reference, given its power stability around O-band, which allows precise characterization of the performance of the optical components and the overall spectrometer system.

For each wavelength, the efficiency is measured. The input TSL beam is first set to the desired wavelength. A spectral density scan is then performed over a sufficiently wide range to include the peak. The resulting spectrum is fitted with a one-dimensional Gaussian profile to extract the peak amplitudes and peak center angles. Ideally, efficiency should remain high and flat, while the peak angle should follow the theoretical calculation.

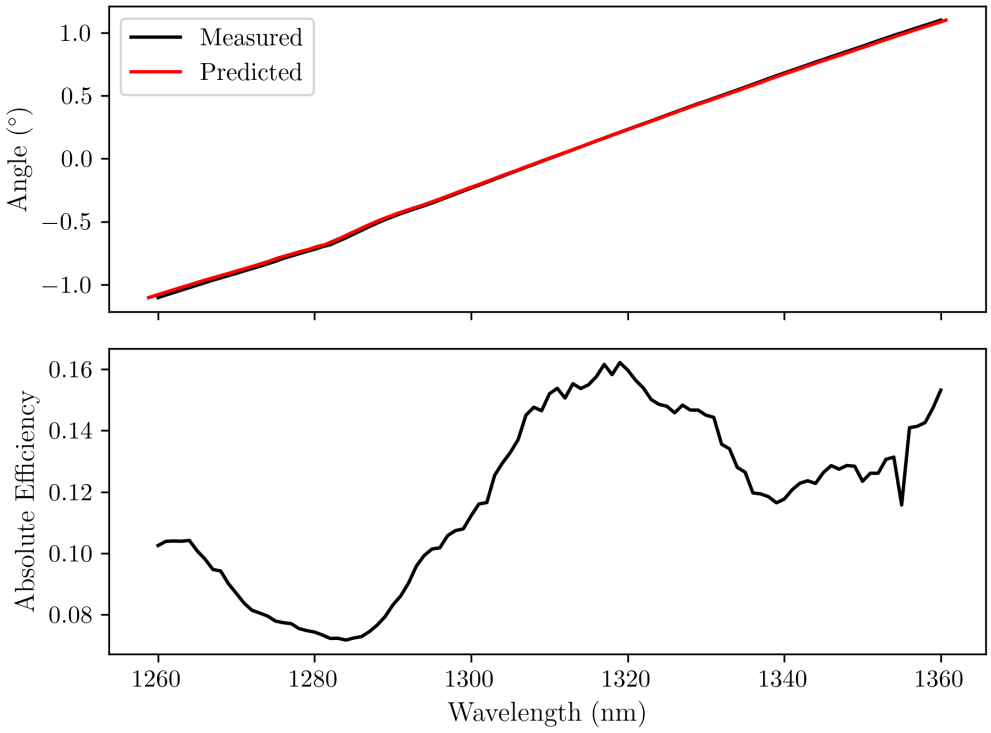


Figure 3.6: Top: Measured and predicted wavelength vs. angle relationship. Bottom: Absolute Detection transmission efficiency vs. wavelength measured.

The measurement results are presented in Figure 3.6. For the angle-wavelength curve, the fitted data points align reasonably well with the theoretical curve with a linear coefficient. However, the efficiency-wavelength curve is not flat. The minimum transmission efficiency, approximately 0.05 at certain wavelengths, indicates potential difficulties in detecting photon-

level signals across the full spectral range, and there is potential to improve this.

## 3.6 Maximize Efficiency by 2-D Scanning

Allowing the two motor angles to differ could help compensate for vertical spatial walk-off and improve beam–collimator coupling efficiency, given the existence of roll errors left unaddressed during spectrometer calibrations.

Based on the concept described above, two-dimensional scans of wavelength data points will be performed using a control script. The procedure is outlined in the following procedure:

```
wavelengths = linear_space(1260, 1360, 51)
scan_slope = 0.021  # approximated dφ/dλ (°/nm) at O-band
for wavelength in wavelengths:
    TSL.set(wavelength=wavelength, intensity=10dB)
    # center angle of 2-D angle map
    center_angle = scan_slope * (wavelength - 1310)
    for left_angle in
        linearspace(center_angle-span/2, center_angle+span/2, 21):
        for right_angle in
            linearspace(center_angle-span/2,
                center_angle+span/2, 21):
             # rotate two motors
            motors.goto(left_angle, right_angle)
            measure_via_PM()
```

This measurement generates a 2-D color map for each wavelength, showing the PM's relative intensity as a function of the left and right motor angles. Examples are shown in Figure 3.7. Ideally, high-transmission-efficiency regions form a diagonal band from the lower left to the upper right. However, the plots show offsets from this pattern, indicating residual misalignment or asymmetries in the spectroscope.

Computing the offset as a wavelength-based Manhattan distance between the local maximum position and theoretical motor angles reveals a sinusoidal pattern (see Figure 3.8). This suggests that transmission efficiency can improve by updating the script rather than adjusting the spectrometer's mechanical calibration.

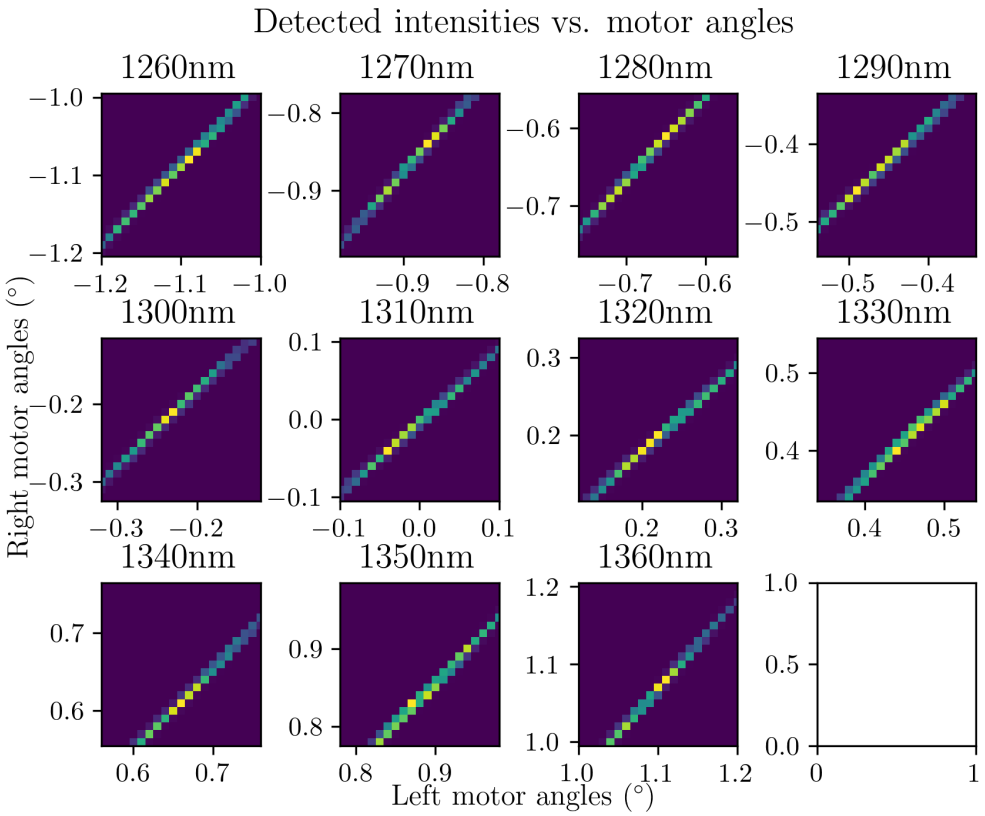


Figure 3.7: Plots showing the measured intensity vs. motor angles under specific TSL working wavelengths. The Viridis color map was used, and brighter areas indicate higher intensity.

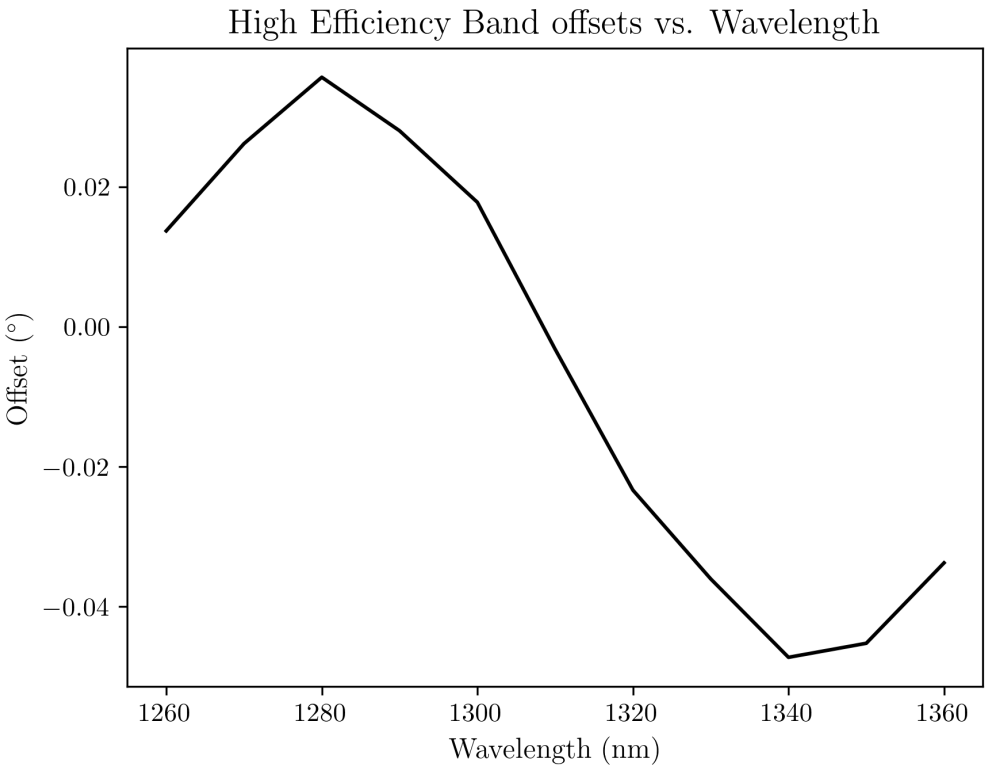


Figure 3.8: The band offset as a function of measured wavelength.

## 3.7 Updated Spectrum Measurement Script

Examining the sampled intensity maps shows that each local maximum corresponds to the motor-angle pair that yields the highest transmission efficiency at that wavelength. The high-efficiency bands in these maps can be modeled as anisotropic two-dimensional Gaussian packets. Similar to the 1-D Gaussian fits used to determine peak centers and heights in wavelength space, a 2-D Gaussian fit in the $(\phi_1,\ \phi_2)$ plane yields the continuous coordinates of the local maximum. For each measured wavelength, this procedure returns $(\phi_{1,\max}, \phi_{2,\max})$; interpolating these pairs across wavelength provides smooth functions $\phi_{1,\max}(\lambda)$ and $\phi_{2,\max}(\lambda)$. The script implementing these steps is outlined

```
# measured data. x and y are motor angles, v is meansured voltage
data = {'1260': [[x], [y], [v]], '1260.2': [...], ...}
wls = list()
angles_max = list()  # motor angles where max v is achieved
for wl in data:
    wls.append(wl)
    x0, y0, A0 = gaussian_2d(*data[w]) # fitting
    angles_max.append([x0, y0])

# given any angle in [1260:1360], returns two angles for measurement.
def wl2angles_interpolate(wl, extrapolation=False):
    assert wl <= 1360 && wl >= 1260
    function_wl2angles = interpolate(wls, angles_max)
    return function_wl2angles(wl)

# updated scanning script
def scan():
    for wl in linspace(1260, 1360, n):
        x, y = wl2angles_interpolate(wl)
        motors.goto(x, y)
        measure_via_APD()
```

The interpolation results and the corresponding relative efficiency color map are presented in Figure 3.9. Using these interpolations, the updated spectrum-scanning script selects motor-angle combinations that yield the highest transmission efficiencies for each wavelength. The color-coded map

shows the optimized efficiencies, which are now flatter across wavelengths, with a minimum of about 0.12, indicating effective sampling and interpolation.

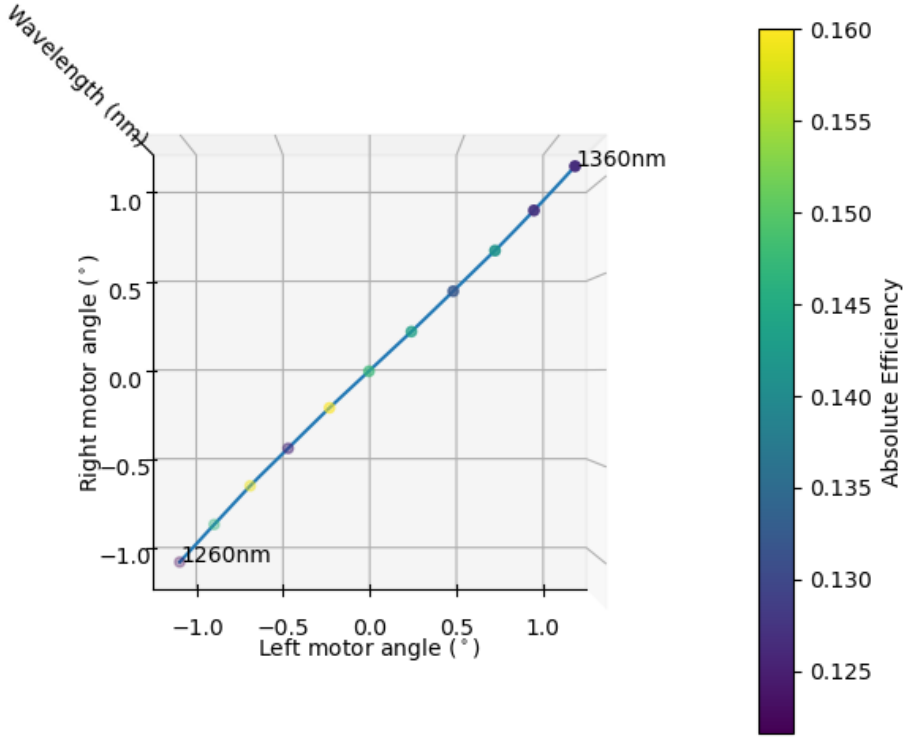


Figure 3.9: The best motor angle pairs coming from fittings and interpolations for each wavelength, with a color map indicating absolute detection efficiency. Here the dots means where the samplings took place.

## 3.8 Collimator Back Reflection Noise

The collimator can introduce noise during measurements due to back reflections from a fiber with a PC connector, which acts as a mirror. This effect worsens as motor angles approach zero alignment center or other specific values.

We first performed a spectral scan of the 1550 nm diode laser with the alignment center set to 1310 nm. Ideally, the resulting curve should exhibit an upward slope similar to that shown in Figure 2.10 assuming no reflective noise is present. However, as illustrated in Figure 3.10, pronounced noise peaks are observed at 1312 nm and 1355 nm. The noise is overwhelming the tail spectral density we want to measure, which is a problem that needs to be addressed.

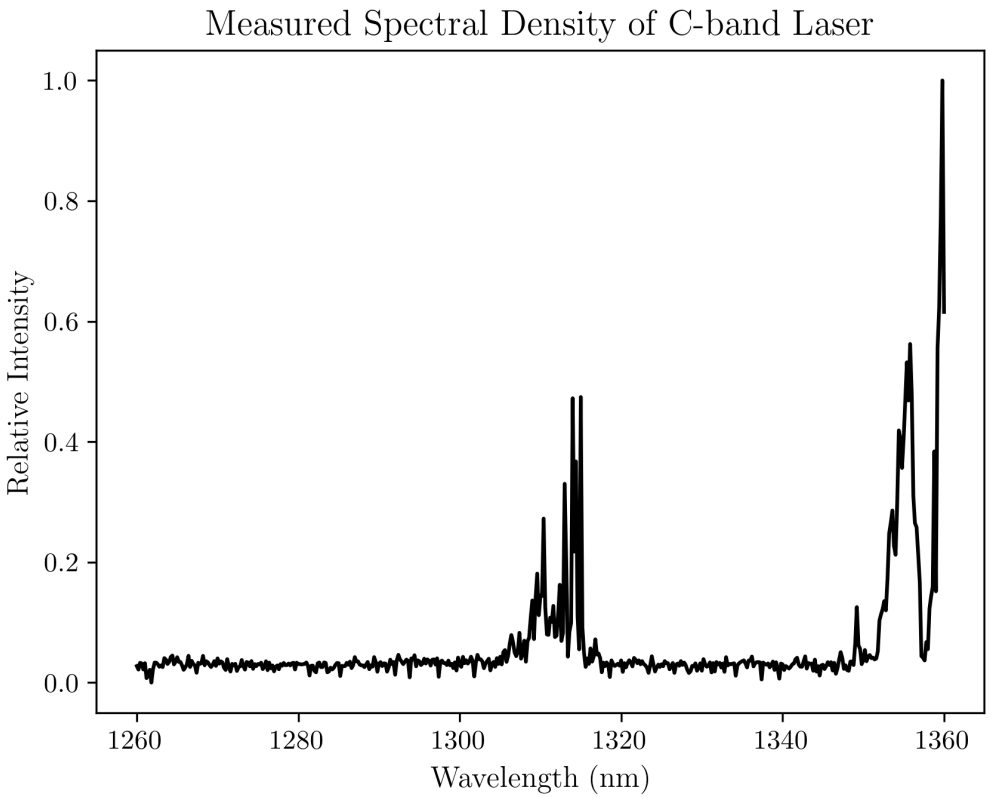


Figure 3.10: Relative spectral intensity for the C-band beam without filtering using the spectrometer, having its alignment done with a 1310 nm reference beam.

To verify whether the photons corresponding to the observed noise peaks indeed originated from the 1550 nm diode laser spectrum peak, a confirmation scan was conducted using the tunable semiconductor laser (TSL). In this measurement, the TSL wavelength was adjusted to each of the wavelengths at which the spectral density had been measured. As shown in Figure 3.11, the measured intensity remained nearly constant, at a level comparable to the APD count noise. This result confirms that the pronounced noise features observed in Figure 3.10 primarily originate from the coherent 1550 nm laser, rather than from external or random noise sources.

Because reflection noise exhibits strong wavelength-dependent coupling determined by the system geometry, the alignment wavelength can be shifted to a region where spectral density measurements are less critical. For example, the alignment can be performed using a 1360 nm coherent beam from the TSL.

Following the alignment procedure and using the transmission efficiency data, a new spectral scan of the C-band beam was performed. The mea-

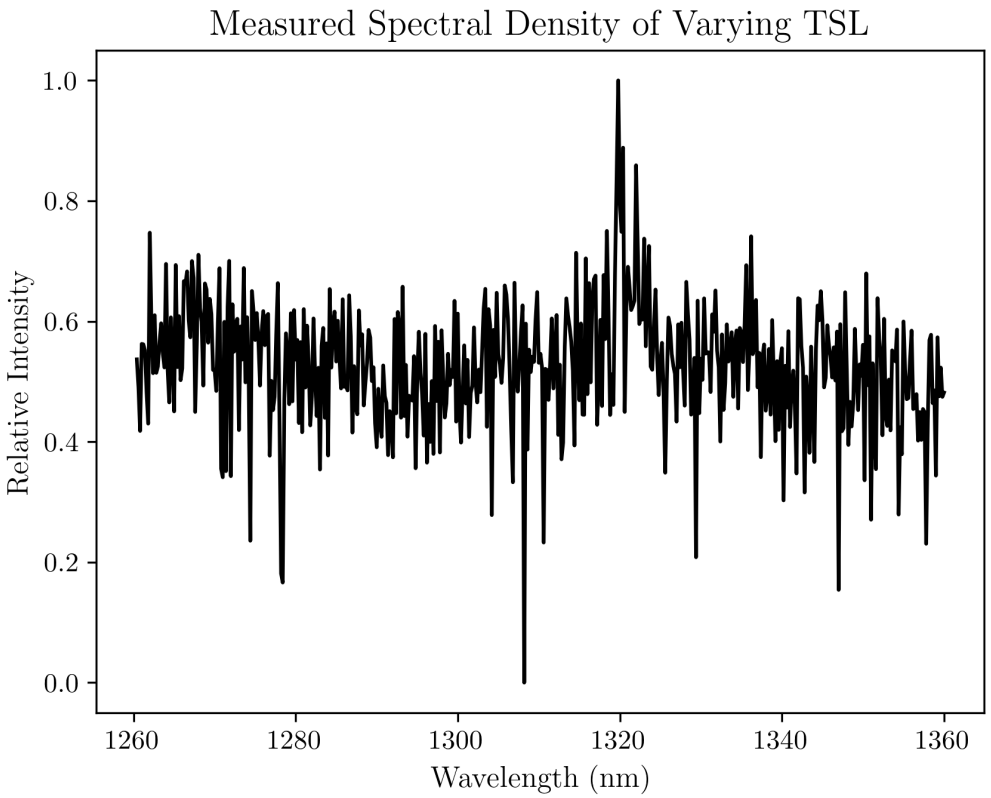


Figure 3.11: Relative spectral intensity for the varying TSL beam without filtering using the spectrometer having its alignment done with a 1310 nm reference beam.

surement in Figure 3.12 shows that the spectrum is less dominated by reflection noise peaks and better reflects the beam's intrinsic tail noise, as referenced to the OSA measurement.

Although reflection-induced noise is still expected to occur near 1360 nm, it is not distinguishable in the spectrum shown in Figure 3.12. In the subsequent filter characterization chapter, we aim further to reduce the tail noise level of the C-band beam, enabling a more decisive verification of the back-reflection noise hypothesis.

In conclusion, back-reflection noise can be effectively compensated by adjusting the wavelength of the reference beam used for grating spectrometer alignment. The strategy is to select a reference wavelength for alignment at which precise spectral intensity measurements are not mandatorily required.

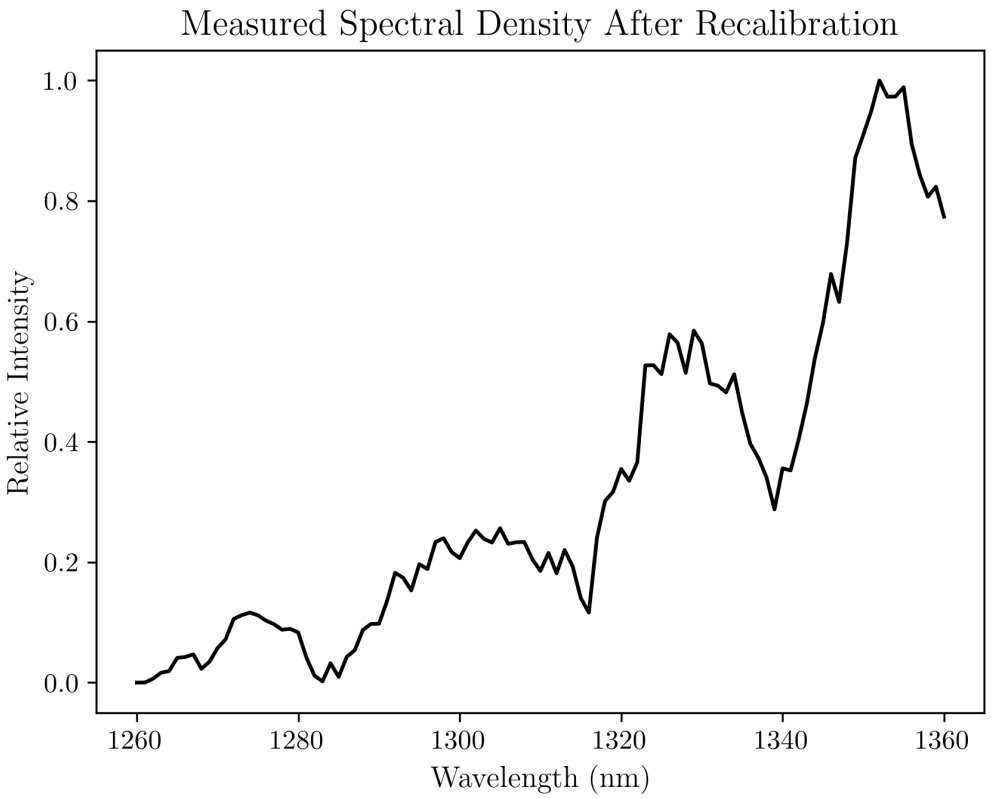


Figure 3.12: Relative spectral intensity for the C-band beam without filtering using the spectrometer, having its alignment done with a 1360 nm reference beam.

## 3.9 Losses and Compensation

Because transmission depends on wavelength, we must identify other factors that reduce efficiency. We aim to create a comprehensive model that accounts for all contributions — constant or state-dependent — and links measured voltage or count rate to the actual spectral intensity. This will enable consistent calibration.

Tracing the optical path, the beam sequentially encounters the input collimator, first grating, first plane mirror, second plane mirror, second grating, and the output collimator with their attenuation denoted as $A_{\text{in}}$, $A_{\text{g1}}$, $A_{\text{m1}}$, $A_{\text{m2}}$, $A_{\text{g2}}$, and $A_{\text{out}}$.

For telecoms wavelengths, $A_{\text{in}}$ they can be treated as constant because reflective collimators exhibit negligible wavelength dependence. The plane mirror factors $A_{\text{m1}}$ and $A_{\text{m2}}$ are also effectively constant within our measurement wavelengths ($< 0.1$ dB). However, the diffraction efficiencies of grating mirrors are both wavelength-dependent and polarization-dependent.

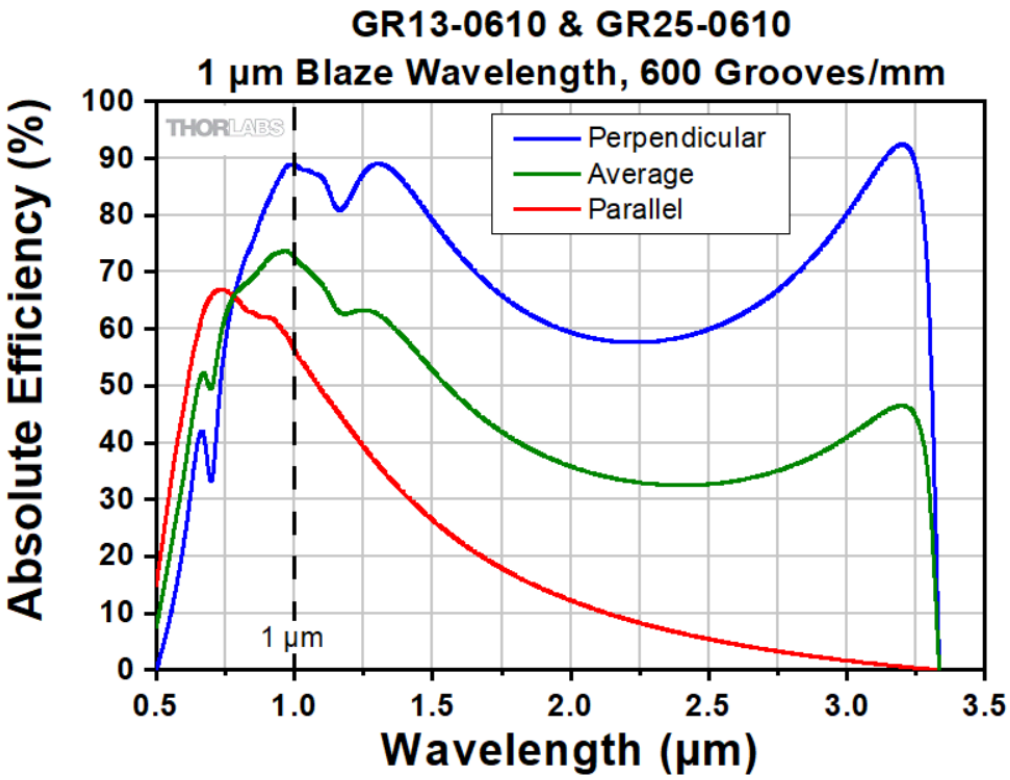


Figure 3.13: The best motor angle pairs coming from fittings and interpolations for each wavelengths, with color map indicating relative intensities. Here the dots means where the samplings took place.

The fiber lengths may affect beam polarization non-uniformly across wavelength, especially when they are long enough ($>$ 10 m). To further understand the mechanism, polarization states across different wavelengths are measured for two lengths: no extra fiber (effectively zero meters as a reference) and a 20 km SMF.

In polarization measurements, the parameters $\phi$ and $\eta$ describe the direction and ellipticity of the polarization ellipse. The polarization ellipse represents the trajectory traced by the electric field vector at a fixed point in space, given by

$$\frac{E_x^2}{E_{0x}^2} + \frac{E_y^2}{E_{0y}^2} - 2\frac{E_x E_y}{E_{0x} E_{0y}} \cos\delta = \sin^2\delta,$$

where $E_{0x}$ and $E_{0y}$ are the field amplitudes in $x$ and $y$ axes, and $\delta$ is the phase difference. The ellipse's orientation angle $\phi$ describes the rotation of its major axis, indicating the dominant polarization direction, and the ellipticity angle $\eta$ quantifies the ratio of the minor to major axes, such that $\tan\eta = b/a$. By measuring the wavelength stability of these two param-

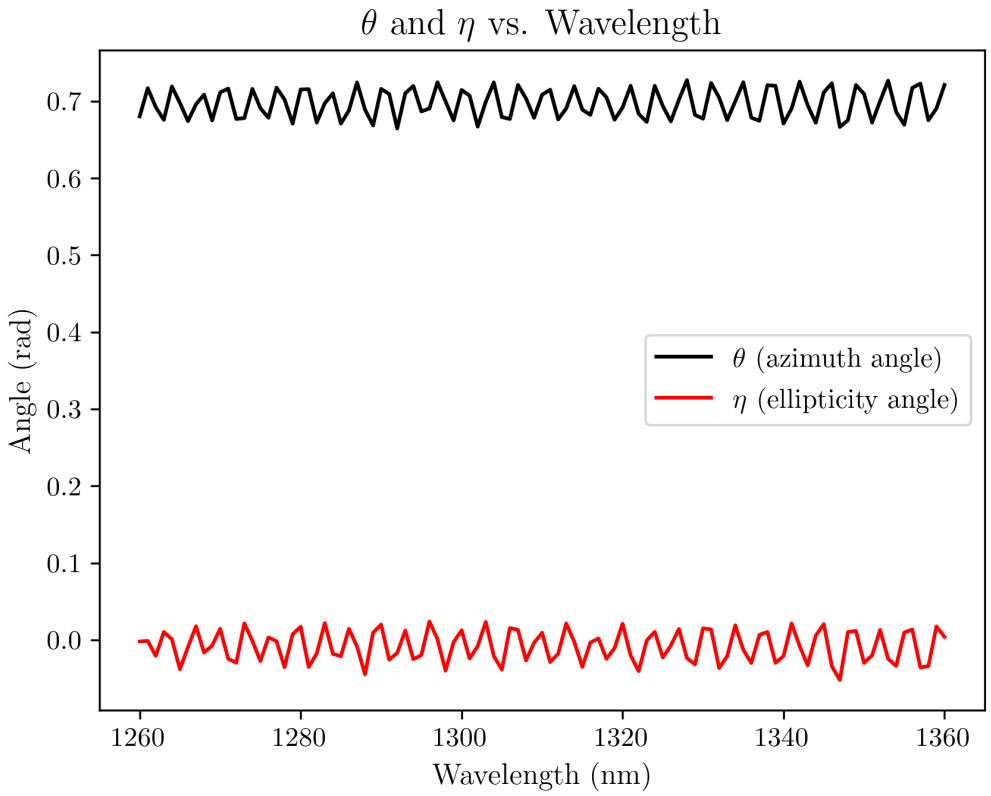


Figure 3.14: Polarization parameters vs. wavelength for a beam without propagating along a long fiber.

eters, one can determine how much a long SMF affects the polarization modes, driven by factors such as birefringence and polarization-mode dispersions.

For the short-fiber case in Figure 3.14, the polarization dependence of wavelength remains relatively stable. The minor fluctuations observed can be attributed to diode instability and instrumental sensitivity. The overall result suggests that at short distances, the polarization state is preserved across wavelengths, consistent with expectations for low-birefringence fibers over limited lengths.

In contrast, for a 20 km fiber, the polarization state measured is shown in Figure 3.15 , which exhibits strong wavelength dependencies. The polarization angle varies significantly across the O-band, indicating cumulative birefringence and mode dispersion along the fiber length. These variations may arise from mechanical stresses due to bending, temperature changes, and fiber-core imperfections. As a result, longer fibers reduce polarization stability during wavelength-dependent measurements and pose a problem when grating mirrors are used.

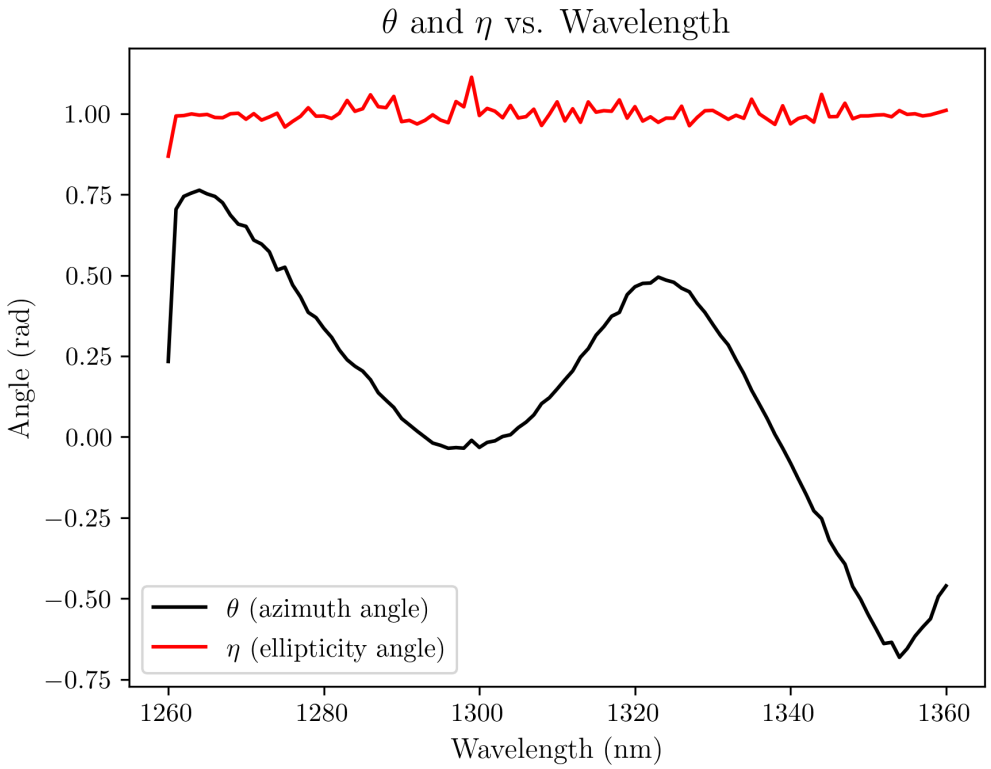


Figure 3.15: Polarization parameters vs. wavelength for a beam after traveling through a 20 km fiber.

However, under the short-fiber approximation, the polarization state can still be assumed constant. Figure 3.13[23] shows that the grating mirror has maximum diffraction efficiency when polarization is perpendicular to the grooves. To address polarization-dependent attenuation, the input polarization is manually adjusted with a fiber polarization controller before each measurement, ensuring the blue curve (perpendicular polarization) is used for post-processing.

The factor $A_{\text{out}}$ depends on the beam-collimator and coupling efficiency. Since this coupling has already been optimized through two-dimensional peak fitting and interpolation, we let $A_{\text{out}} = A_{\text{out}}(\lambda)$ a function determined by the efficiency presented in Figure3.9.

Finally, the total attenuation is

$$A_{\text{tot}} = A_{\text{in}}\, A_{\text{m1}}\, A_{\text{m2}}\, A_{\text{g1}}(\lambda)\, A_{\text{g2}}(\lambda)\, A_{\text{out}}(\lambda). \tag{3.21}$$

Taking $\lambda = 1310$ nm as an example, the value of $A_{\text{tot}}$, according to measurements, equals 19.37%.

## 3.10 Summary

In this chapter, we discussed the design, construction, and calibration of a cascaded grating spectrometer, which theoretically reduces C-band leakage. Due to the complexity of numerically relating motor angles to measured wavelengths, given alignment errors, a TSL was introduced to experimentally verify how well the proposed model describes the grating spectrometer's behavior.

Subsequently, TSL-based testing shows that the detection efficiency strongly depends on the target wavelength. To address this, we explored methods to optimize the efficiency behavior by abandoning the symmetric angle assumption and significantly improving both the magnitude and stability of the transmission efficiency. The optimal angle pairs for each wavelength can be determined by performing 2-D scan samplings followed by interpolation across the measured data.

Finally, to achieve more accurate quantitative measurements, the factors contributing to efficiency loss during beam propagation in the grating spectrometer were analyzed. The calculated overall attenuation will be applied to the measured spectrum to compensate for all modeled sources of optical losses in the spectrometer during data analysis.

# Chapter 4

# Noise Filtering

## 4.1 Noise from Transmission

Filters are required on the transmission side in co-propagating QKD systems. The architecture illustrated in Figure 1.1 includes a media converter on the left that encodes classical bits into photons at a wavelength of 1550 nm. Beside this converter is a coherent light source operating at 1310 nm, in which the quantum state $|\Psi\rangle$ is encoded. The two independent optical sources are combined using a wavelength-division multiplexer (WDM), allowing both signals to propagate simultaneously through the same fiber.

However, a problem arises when another WDM demultiplexes the co-propagating signal on the receiving side. Similar to the C-band diode laser used in our setup, the media converter's emission spectrum is not ideally confined to a delta function at its nominal operating wavelength; instead, it exhibits significant intensity far from the peak. Photons carrying classical information having wavelengths near 1310 nm may enter the same port of the receiving WDM that is designated for photons carrying quantum information[24]. This leakage introduces noise, degrading the signal-to-noise ratio (SNR). The process is illustrated schematically in Figure 4.1, where the noise level is overwhelming the signal at the 1310 nm WDM output port.

Several approaches can be proposed to lower the transmission noise. One option is to place a filter after the media converter to block photons with wavelengths near 1310 nm, thereby reducing spectral leakage reaching

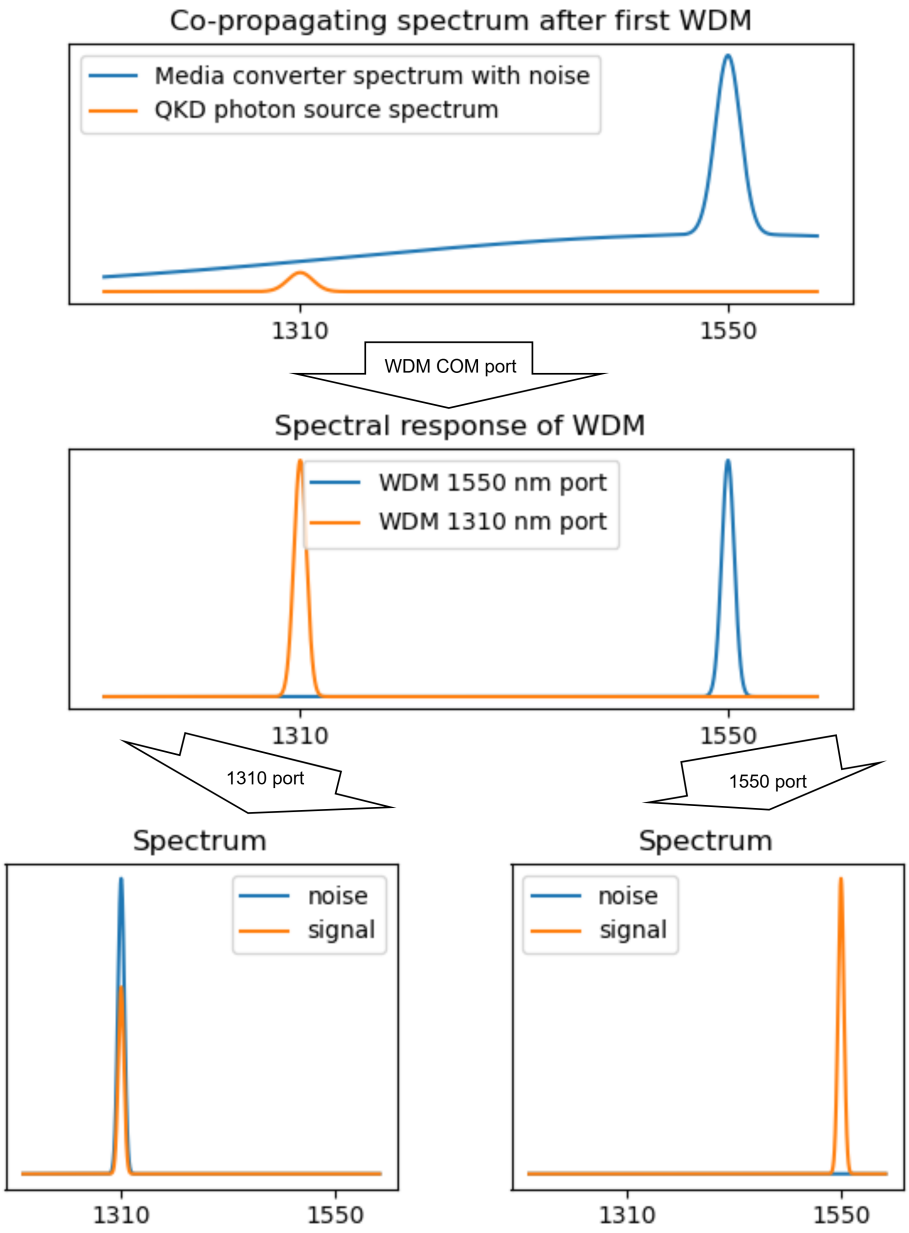


Figure 4.1: Top: Spectrum of two sources co-propagating in the fiber between two WDMs. Middle: Spectral response function of two ports on an ideal WDM. Bottom: Output spectrum of two WDM ports.

the single-photon detector. However, this method assumes that the WDM exhibits an ideal spectral response function: the optical density (OD) is high ($> 8$) for all wavelengths except the designated output channels. Since this assumption requires further verification, filtering out only a narrow spectral band may not be the most reliable approach.

An alternative method is to use a band-pass filter after the media converter, allowing only photons within a narrow wavelength range centered around 1550 nm to pass without significant attenuation. This approach filters the output more effectively and minimizes cross-effects between the classical and quantum channels.

The response functions of various filtering profiles can be evaluated to determine which are most effective in reducing transmission noise. This analysis can be conducted using the constructed spectrometer together with the scanning script. In the following sections, we discuss the characteristics and performance of the wavelength-division multiplexer (WDM), the dense wavelength-division multiplexer (DWDM), and the free-space band-pass filter.

## 4.2 (D)WDM and Band Pass Filter

### 4.2.1 (D)WDM

In addition to their roles in multiplexing and demultiplexing, WDMs can also contribute to tail noise suppression through their wavelength selectivity.

Typically, WDMs are used in pairs to enable the co-propagation of classical signals rather than for filtering single-photon-level noise. Therefore, measurements are necessary to characterize their spectral response, particularly around 1310 nm. A straightforward approach is to send a C-band beam and measure the spectral density at the output to assess the amount of leakage after filtering. However, since the tail noise level varies with wavelength, an alternative and more accurate method is to use the TSL to perform a wavelength scan, similar to the procedure used for estimating the transmission efficiency of the cascaded grating spectrometer.

According to the WDM operating principle, the TSL output goes to the WDM's COM port, and spectral intensity is measured at the C-band

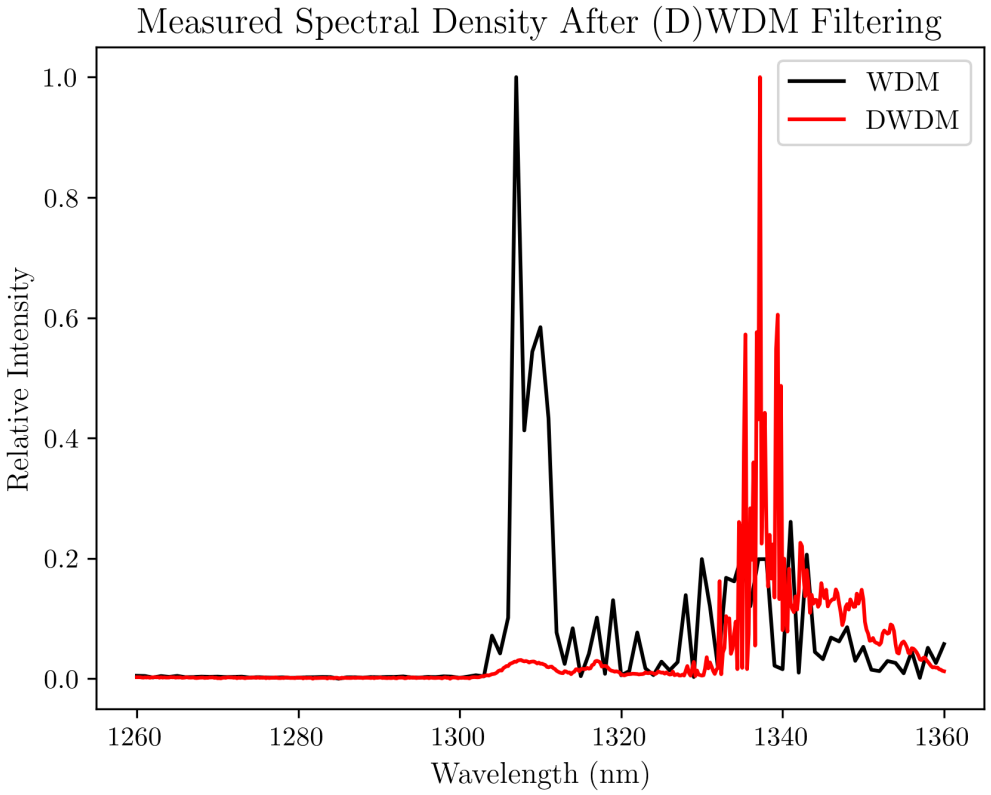


Figure 4.2: TSL relative spectral density when filtered by a WDM or DWDM.

output. To determine OD at a specific wavelength, the TSL is set to that wavelength with constant output intensity. The grating mirrors rotate based on the wavelength-angle relationship, and any attenuation in the signal is compensated to enhance accuracy. Using these measurements, the relative wavelength-dependent optical density of the WDM can be calculated.

In Figure 4.2, which shows the measured spectral response of the WDM, the optical density should stay nearly constant across the wavelength range. However, results show otherwise, with increased photon leakage in certain spectral regions, especially around 1310 nm. This leakage affects filtering noise in co-propagating QKD systems. Even with ideal WDMs, reduced attenuation in these regions allows more photons from the classical channel to leak into the quantum channel. If leaked photons outnumber the quantum signal at the detector, it could raise the QBER.

To further investigate the phenomenon, a dense wavelength-division multiplexer (DWDM) was tested under similar conditions. The DWDM used is primarily designed for the C-band, having eight narrowly spaced

channels centered around 1550 nm. Its spectral characteristics in the O-band are not defined by its design, so evaluating its response in this range provides valuable insight into its out-of-range behavior. If the DWDM exhibits similar irregular attenuation near the O-band, the leakage is more likely due to the WDMs. According to the curve for DWDM in Figure 4.2, the measured transmission spectrum of the DWDM was obtained from a wavelength-swept scan. Given its finer spectral division, the DWDM provides a valuable means to distinguish whether the previously observed leakage originates from the WDM device's specific design or from wavelength-dependent propagation effects along the optical path.

Spectral inconsistencies likely stem from the design limitations of commercial (D)WDM devices, which are optimized for standard output wavelengths. At intermediate wavelengths, performance degrades, leading to reflections and spectral leakage.

### 4.2.2 Band-Pass Filter

To find a feasible way of suppressing the spectral leakage and tail noise observed in Figure 3.12, a free space band-pass filter with an optical density exceeding six outside its passband was added after the diode laser. The filter is designed to have a narrow transmission spike centered at 1550 nm, ensuring that only photons within this region are transmitted, while all others are attenuated. This configuration effectively purifies the signal wavelength from broadband background light and other potential noise sources in the transmission direction.

When the C-band diode laser spectrum was measured after passing through the free space band-pass filter, the resulting transmission spectrum in Figure 4.3 demonstrates that the filter effectively suppresses tail noise outside its designed passband. The spectral intensity remains flat and indistinguishable from the APD dark count within the $1310 \pm 30$ nm range, indicating that background noise has been reduced to the detection limit, consistent with the off-band optical density of 6.

Spectral peaks around 1265 nm and 1360 nm are attributed to weak back reflections from the collimator surfaces. As previously discussed, these peaks were not visible in Figure 3.12 because they were overwhelmed by the tail noise. However, after having the band-pass filter, they become

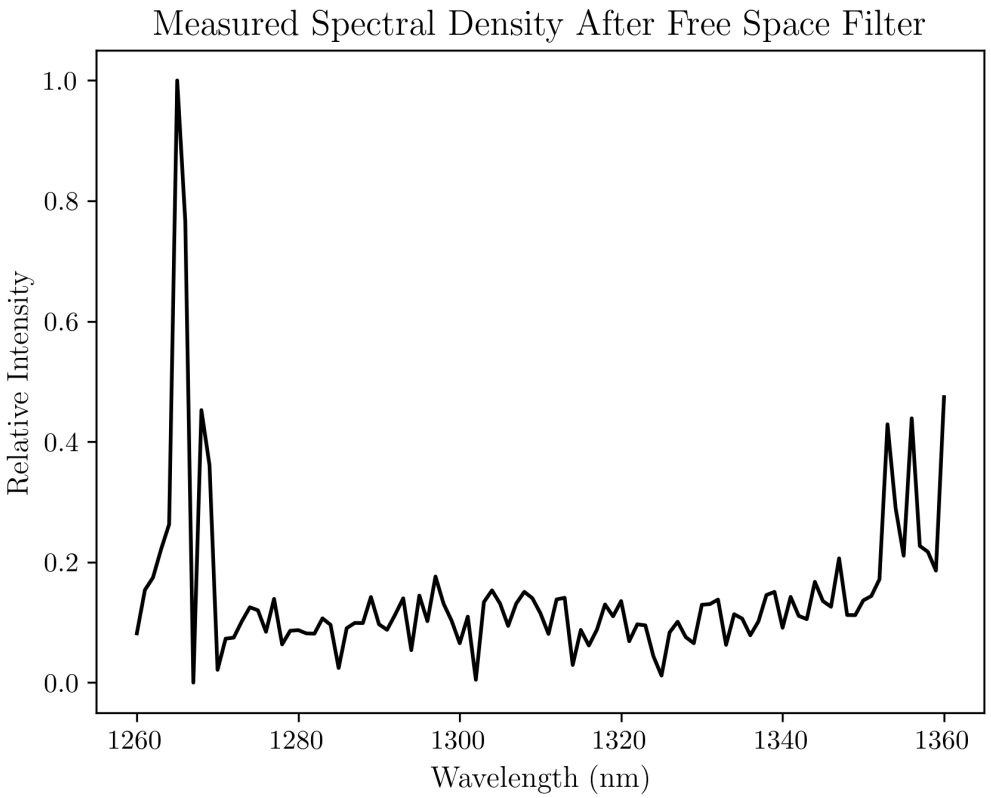


Figure 4.3: Relative tail spectral density measured for the C-band beam when filtered by a band pass filter.

distinguishable. Since their positions correspond to the known collimator back reflection effect, these peaks can be safely ignored in the spectral analysis.

In conclusion, the chosen band-pass filter filters broadband tail noise while preserving the beam's coherence. It will be a valid method for tail-noise suppression, reducing transmission noise.

## 4.3 Properties of Raman Scattering

The filtering efforts described so far have primarily focused on eliminating tail noise induced by the C-band laser source to the media converter before it enters the co-propagating fiber. However, even if the classical channel exhibits an ideal spectral profile after filtering, the possibility of its photon leaking into the O-band, where the quantum signals propagate, remains.

The leakage arises not from imperfections in the light source itself, but from the properties of the optical fiber used for co-propagation. Nonlinear processes such as spontaneous Raman scattering[5] and four-wave mixing

within the fiber can up-convert a small fraction of C-band photons toward shorter wavelengths, including those within the O-band window. These factors can introduce additional background photons into the quantum channel, forcing us to evaluate the fiber-related spectral modifications.

To establish reference points for the following scattering analysis, two baselines were defined. The first corresponds to a zero kilometer case, represented by the tail spectrum measurement after the band-pass filter shown in Figure 4.3. The second baseline involves transmission through a 20 km telecoms SMF, which serves as the reference for evaluating fiber-induced scattering intensity. In both cases, a C-band coherent diode laser with an output power of approximately 3 mW after filtering was used as the input source.

Three major factors potentially related to in-fiber scatterings are

- Fiber length, which accumulates scattered photons.
- Input power shifting scattering intensity.
- Role of input polarization state on scattering.

These measurements provide evidence of how fiber properties can influence the amount and spectrum of unwanted photon generation, thereby characterizing the transmission noise due to beam propagation in fiber.

The first set of measurements tests how increasing fiber length affects the amount of scattering detected around the O-band. The attenuation due to fiber length was linearly compensated, yielding a spectrum that represents the relative scattering.

The results plotted in Figure 4.4 show that the number of scattered photons increases linearly when the fiber length goes from 10 km to 20 km , but appears to rise super-linearly when the length increases from 20 km to 50 km. The reason could have been the cumulative nature of spontaneous Raman scattering and the re-scattering of the photons it generates. In summary, we say that while the scattering process is approximately linear for short fiber lengths, secondary effects may cause it to grow super-linearly[25] when the length exceeds several tens of kilometers.

The second part of the characterization tests how the C-band laser intensity affects the scattering around the O-band. The same VOA we have been using for APD detection was used to modulate the input power. The

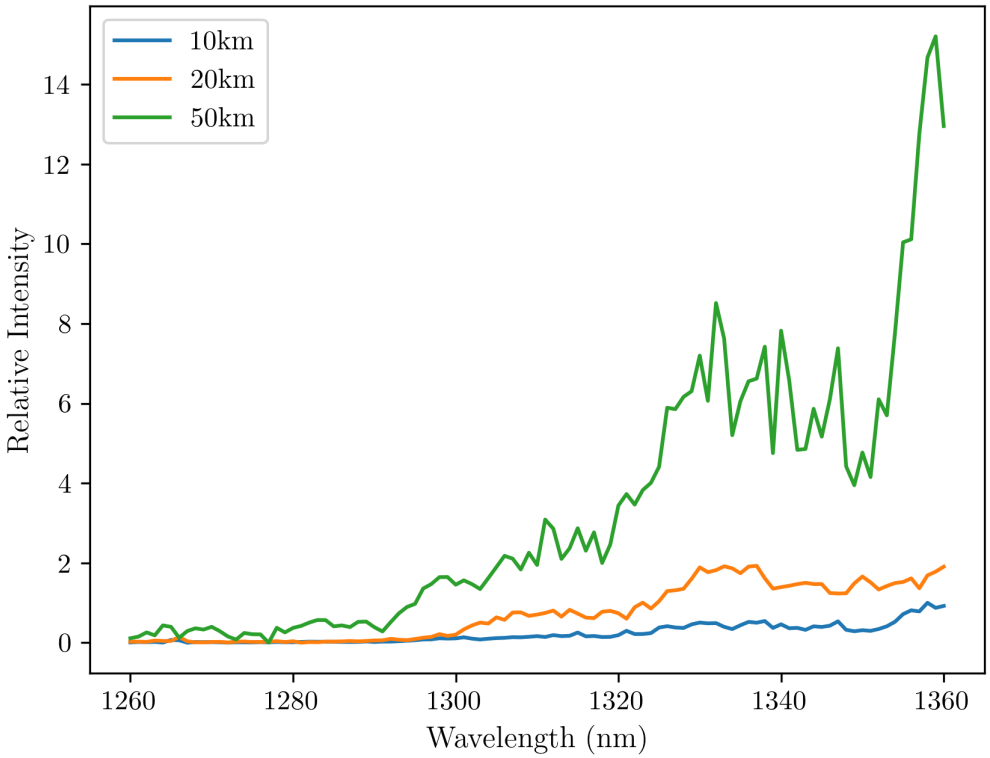


Figure 4.4: Measured relative spectral density after transmission through long segments of SMF. The y-axis has been linearly scaled to the corresponding fiber attenuation, highlighting variations in scattering intensity rather than absolute power loss.

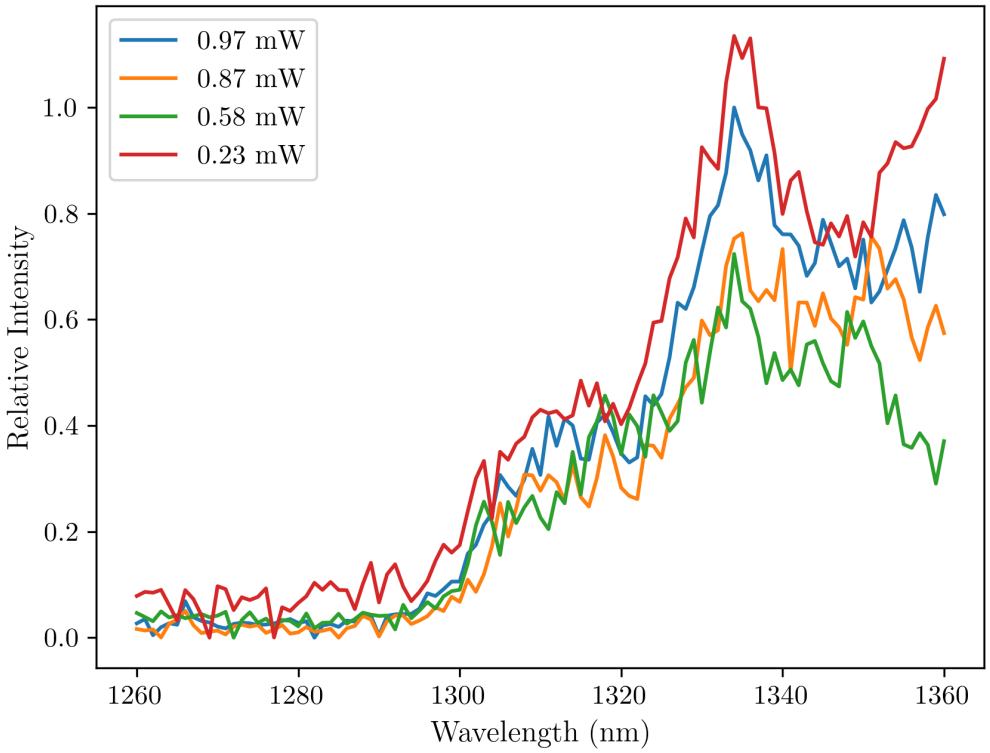


Figure 4.5: Measured relative spectral density with different pump power. The y-axis has been linearly scaled according to the VOA attenuation. The fiber length used is 20 kilometers.

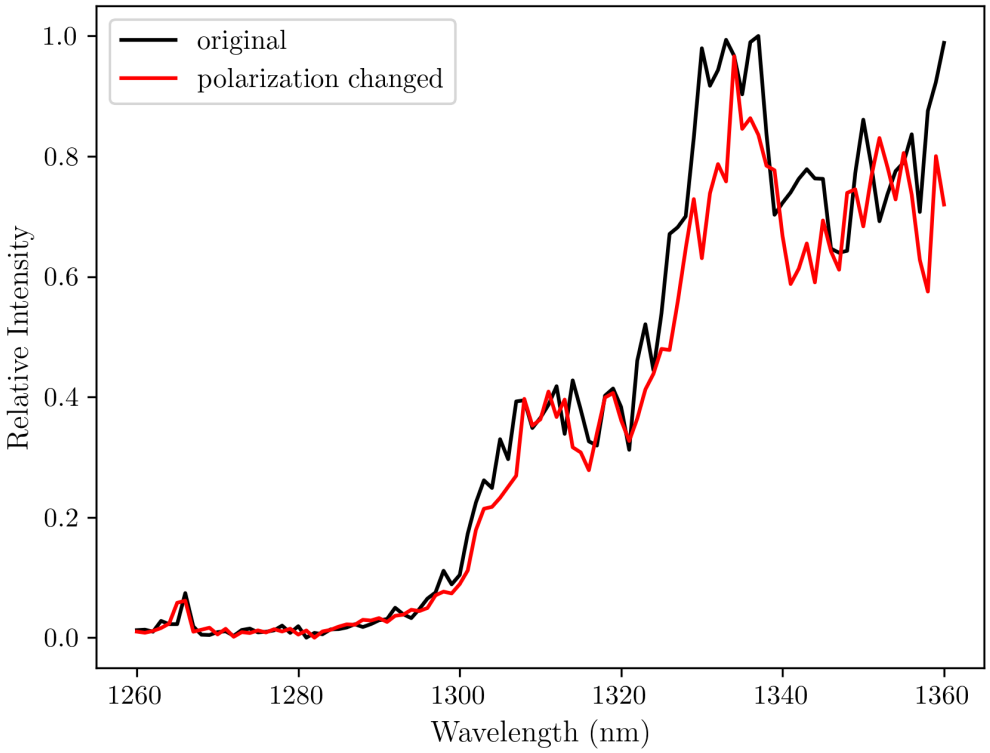


Figure 4.6: Measured relative spectral density for different polarizations due to fiber stress.

resulting spectra in Figure 4.5 show that as the pump power decreases, the overall amplitude of the scattered signal decreases proportionally. This observation aligns with the theoretical expectation that the strength of spontaneous Raman scattering is linearly dependent on the input optical power. After compensating for the VOA attenuation, the relative spectrum display shows similar shapes across applied voltages, indicating that the scattering process is highly power-dependent. The results confirm that Raman noise around the O-band scales directly with the classical channel intensity, implying that reducing the C-band intensity can help decrease the QBER in co-propagating QKD systems.

The third measurement examines how fiber-induced polarization changes (see Figure 3.15 for visualization) affect the spectral intensity of scattering. Mechanical stress applied to 20 km of SMF induced a polarization perturbation by altering birefringence, thereby changing the polarization state. Figure 4.6 shows spectra before and after this perturbation, which remain nearly identical with minor amplitude changes, indicating minimal impact on spontaneous Raman scattering. Fluctuations are likely due to polarization-dependent losses at connectors and bends, as well as varia-

tions in grating mirror efficiency. In conclusion, changes in polarization induced by mechanical stress in the fiber do not significantly destabilize transmission noise levels.

## 4.4 Proposed Filtering Scheme for Transmission Noise

In a co-propagating QKD architecture, as illustrated in Figure 1.1, two sources of transmission noise have been characterized. The first one originated from the spectral tail of the transmit source media converter, whose emission extends toward shorter wavelengths such as 1310 nm. This tail leakage results in photons entering the quantum channel, and they are indistinguishable from quantum photons. The second primary source comes from the co-propagating fiber: spontaneous Raman scattering is the dominant process generating photons throughout the O-band when the C-band classical signal (even with perfect spectral behavior) propagates over long distances. Both mechanisms increase the number of noise photons reaching the APD, thereby reducing the signal-to-noise ratio and corrupting the QBER.

The first type of transmission noise occurs before the signal even enters the shared fiber. Filtering should be applied immediately after the media converter's optical output to reduce it. The most effective method is to add a narrow-band band-pass filter centered at 1550 nm with high optical density (OD>6) when outside its passband; cascade the same filtering if necessary, as long as the attenuation level remains acceptable. This filter narrows the spectrum to a peak around the designated wavelength and removes tail noise.

These together create spectral purification on the transmitter side, ensuring that the light entering the co-propagating fiber carries minimal off-band photons. The trade-off is increased insertion loss or free-space coupling loss, which is acceptable given a sufficient reduction in the noise level reaching the receiver to avoid potentially blinding the APD.

The second source of noise comes from the transmission medium. Spontaneous Raman scattering intensity increases with both the input optical power of the classical channel and the fiber length. Mitigation should focus on controlling the power that travels through the fiber and filtering at the

receiver to reject scattered photons outside 1310 nm.

On the transmitter side, power management is the simplest solution. Keeping the classical intensity low enough while ensuring the signal is detectable at the receiver's media converter linearly reduces Raman-related photon generation. After the de-multiplexing (D)WDM, an O-band bandpass filter centered at 1310 nm needs to be installed before the APD to reject residual signals.

## 4.5 Backward Noise Estimation

In addition to the forward noise discussed earlier, co-propagating QKD can be affected by backward-propagating noise. Such noise originates primarily from two sources

- Back-reflected light from the receiver-side media converter due to imperfect WDM
- Backward Raman scattering[26] occurring within the shared fiber

Although these effects are expected to be weaker than their forward counterparts, their influence becomes non-negligible when the system operates at photon-sensitivity levels. Filtering designs must be added along backward noise-propagation paths to ensure fewer stray photons reach the APD input via reverse optical coupling.

Back-reflections can arise at multiple points in the receiver module, including fiber connectors, circulators, collimators, and even in the optical interfaces of the media converter. Given that the converter operates at the micro-level of optical power, due to attenuation applied to reduce forward scattering, a reflection coefficient of approximately $-60$ dB is sufficient to bring $10^{-12}$ W the signal into the quantum channel. These reflected photons can re-enter the fiber and, after multiple scattering or WDM imperfections, reach the APD. The effect is most pronounced when the wavelength of the reflected light matches the proposed detection band near 1310 nm, especially in the absence of additional isolation elements.

Backward Raman scattering is an intrinsic nonlinear process in which some of the backward-propagating C-band light emitted by the receiver-side media converter is scattered into the forward direction. This mechanism

generates photons that can eventually reach the APD. Its intensity scales via the same parameters as the forward Raman process, including classical optical power and fiber length, but it may have a different spectral distribution.

Though the intensity of backward noise depends on the reflectivity and scattering coefficients of the optical components, its magnitude can be estimated by extending the known Raman relationships from forward-propagating characteristics[27]. Usually, for SMFs, the backward-forward Raman scattering ratio is typically around 10%. Assuming a classical launch power of 30 $\mu$W and a fiber length of 20 km, the backward Raman intensity reaching the receiver port can be estimated to be on the order of $10^6$cps, corresponding to about $10^4$cps detected by the APD. This level is comparable to that of the APD dark count. If unfiltered, it could increase the QBER by several percent, especially in systems without temporal gating.

## 4.6 Backward Noise Mitigation

Additional isolation elements can be deployed at key points in the architecture to suppress backward noise. The most effective approach is introducing an optical isolator immediately after the quantum-channel WDM on the transmitting side. This isolator allows forward propagation of the quantum signal while attenuating any backward ones. A second isolator can be placed after the receiver-side WDM to prevent reflections from the media converter from re-entering the shared fiber.

For even better noise suppression, we prefer using angled physical contact (APC) fiber connectors wherever reflection reduction matters to reduce reflections at fiber interfaces.

Additionally, the level of backward Raman scattering can be decreased by reducing the optical power emitted from the TX port of the receiver-side media converter. This method follows the same principle used to suppress forward Raman scattering: reducing the classical optical intensity proportionally decreases the number of photon-generation events in the shared fiber.

## 4.7 Summary

Building on previous discussions of forward and backward noise filtering to enhance QKD quality, the overall co-propagating architecture becomes a comprehensive multistage noise-cancellation system in both directions. Forward transmission noise is reduced through spectral filtering at the source and Raman suppression, while backward noise is minimized via optical isolation and reflection control. Collectively, these methods decrease the number of unwanted photons reaching the APD in lab components.

# Chapter 5

# Conclusion

This work presents investigations on the feasibility and optimization of co-propagating QKD, focusing on the characterization and mitigation of optical noise in shared-fiber environments. Through both theoretical analysis and experimental implementation, the study identifies and quantifies the main challenges arising: tail emission from classical transmitters, spontaneous Raman scattering in the fiber, and back-reflection from optical interfaces.

To enable precise noise evaluation, a high-resolution grating-based spectrometer was deployed and validated. The instrument's design evolution from a single-grating to a cascaded one has improved spectral selectivity, dynamic range, and sensitivity to photon-counting levels. Experimental calibration using a tunable laser source confirmed wavelength-dependent transmission efficiency and revealed optical attenuation mechanisms associated with polarization and geometrical alignment.

After that, we compared multiple noise-filtering components, including wavelength-division multiplexers (WDM/DWDM) and free-space bandpass filters, and estimated their limitations and applicable spectral regions. Measurements across 10–50 km fiber further confirmed that spontaneous Raman scattering scales approximately linearly with both fiber length and optical power but exhibits nonlinear growth beyond several tens of kilometers. By combining these filters, the signal-to-noise ratio can be significantly improved. These findings provide both a quantitative and architectural foundation for designing practical co-propagating DVQKD systems capable of secure operation in existing telecom infrastructures.

Future research extends the current analysis to refined estimations of backward Raman scattering, combined with systematic estimations of back-reflected light from the receiver side, forming a complete noise map in co-propagating architectures. Furthermore, integrating new filters, active polarization stabilization, and real-time spectrum monitoring could help in long-term system stability.

# Bibliography


[1] Thiago Ferreira da Silva et al. "Impact of Raman Scattered Noise from Multiple Telecom Channels on Fiber-Optic Quantum Key Distribution Systems". In: *Journal of Lightwave Technology* 32.13 (July 2014), pp. 2332–2339. ISSN: 1558-2213. DOI: 10.1109/jlt.2014.2322108. URL: http://dx.doi.org/10.1109/JLT.2014.2322108.

[2] Fabian Laudenbach et al. "Continuous-Variable Quantum Key Distribution with Gaussian Modulation—The Theory of Practical Implementations". In: *Advanced Quantum Technologies* 1.1 (2018), p. 1800011. DOI: https://doi.org/10.1002/qute.201800011. eprint: https://advanced.onlinelibrary.wiley.com/doi/pdf/10.1002/qute.201800011. URL: https://advanced.onlinelibrary.wiley.com/doi/abs/10.1002/qute.201800011.

[3] Adnan A. E. Hajomer et al. "Coexistence of Continuous-Variable Quantum Key Distribution and Classical Data over 120 km Fiber". In: *Phys. Rev. Lett.* 135 (17 Oct. 2025), p. 170804. DOI: 10.1103/zy2d-m3ch. URL: https://link.aps.org/doi/10.1103/zy2d-m3ch.

[4] S. Pirandola et al. "Advances in quantum cryptography". In: *Adv. Opt. Photon.* 12.4 (Dec. 2020), pp. 1012–1236. DOI: 10.1364/AOP.361502. URL: https://opg.optica.org/aop/abstract.cfm?URI=aop-12-4-1012.

[5] H. Kawahara, A. Medhipour, and K. Inoue. "Effect of spontaneous Raman scattering on quantum channel wavelength-multiplexed with classical channel". In: *Optics Communications* 284.2 (2011), pp. 691–696. ISSN: 0030-4018. DOI: https://doi.org/10.1016/j.optcom.2010.09.051. URL: https://www.sciencedirect.com/science/article/pii/S0030401810010199.

[6] Yingqiu Mao et al. "Integrating quantum key distribution with classical communications in backbone fiber network". In: *Opt. Express* 26.5 (Mar. 2018), pp. 6010–

6020. DOI: 10.1364/OE.26.006010. URL: https://opg.optica.org/oe/abstract.cfm?URI=oe-26-5-6010.

[7] Pierre-Enguerrand Verdier, Romain Alléaume, and Thomas Rivera. "Investigating Raman backscattering decay and the perspective of time-multiplexed quantum communications". In: *Opt. Express* 33.15 (July 2025), pp. 31029–31041. DOI: 10.1364/OE.561961. URL: https://opg.optica.org/oe/abstract.cfm?URI=oe-33-15-31029.

[8] Ryan Allured and Randall T. McEntaffer. "Analytical alignment tolerances for off-plane reflection grating spectroscopy". In: *Experimental Astronomy* 36.3 (Sept. 2013), pp. 661–677. ISSN: 1572-9508. DOI: 10.1007/s10686-013-9349-y. URL: http://dx.doi.org/10.1007/s10686-013-9349-y.

[9] William M. Holden et al. "A compact dispersive refocusing Rowland circle X-ray emission spectrometer for laboratory, synchrotron, and XFEL applications". In: *Review of Scientific Instruments* 88.7 (July 2017), p. 073904. ISSN: 0034-6748. DOI: 10.1063/1.4994739. eprint: https://pubs.aip.org/aip/rsi/article-pdf/doi/10.1063/1.4994739/14789479/073904_1_online.pdf. URL: https://doi.org/10.1063/1.4994739.

[10] Thorlabs. *K10CR1 - Motorized Rotation Mount for Ø1" Optics, Stepper Motor, Imperial*. Accessed: 2025-11-3. 2024. URL: https://www.thorlabs.com/thorproduct.cfm?partnumber=K10CR1.

[11] Cristine Calil Kores et al. "Temperature dependence of the spectral characteristics of distributed-feedback resonators". In: *Opt. Express* 26.4 (Feb. 2018), pp. 4892–4905. DOI: 10.1364/OE.26.004892. URL: https://opg.optica.org/oe/abstract.cfm?URI=oe-26-4-4892.

[12] Il Ku Kim et al. "Detectivity analysis for organic photodetectors". In: *Organic Electronics* 57 (2018), pp. 89–92. ISSN: 1566-1199. DOI: https://doi.org/10.1016/j.orgel.2018.02.036. URL: https://www.sciencedirect.com/science/article/pii/S1566119918300909.

[13] John H. Scofield. "Frequency-domain description of a lock-in amplifier". In: *American Journal of Physics* 62.2 (Feb. 1994), pp. 129–133. ISSN: 0002-9505. DOI: 10.1119/1.17629. eprint: https://pubs.aip.org/aapt/ajp/article-pdf/62/2/129/11441741/129_1_online.pdf. URL: https://doi.org/10.1119/1.17629.

[14] Dobromir Dobrev, Tatyana Dobreva, and Nikolay Mudrov. "Digital lock-in techniques for adaptive power-line interference extraction". In: *Physiological measurement* 29 (Aug. 2008), pp. 803–16. DOI: 10.1088/0967-3334/29/7/009.

[15] Chen Liu, Hai-Feng Ye, and Yan-Li Shi. "Advances in near-infrared avalanche diode single-photon detectors". In: *Chip* 1.1 (2022), p. 100005. ISSN: 2709-4723. DOI: https://doi.org/10.1016/j.chip.2022.100005. URL: https://www.sciencedirect.com/science/article/pii/S270947232200003X.

[16] K.A. Patel et al. "Gigacount/second photon detection with InGaAs avalanche photodiodes". In: *Electronics Letters* 48.2 (Jan. 2012), pp. 111–113. ISSN: 1350-911X. DOI: 10.1049/el.2011.3265. URL: http://dx.doi.org/10.1049/el.2011.3265.

[17] Ioannis Argyriou et al. "The nature of point source fringes in mid-infrared spectra acquired with the James Webb Space Telescope". In: *Astronomy & Astrophysics* 641 (Sept. 2020), A150. ISSN: 1432-0746. DOI: 10.1051/0004-6361/202037535. URL: http://dx.doi.org/10.1051/0004-6361/202037535.

[18] Xunyu Li, Jens Riedel, and Yi You. "Practical high-resolution spectroscopy with a spatial heterodyne spectrometer: Determination of instrumental function for lineshape recovery". In: *Spectrochimica Acta Part B: Atomic Spectroscopy* 221 (2024), p. 107053. ISSN: 0584-8547. DOI: https://doi.org/10.1016/j.sab.2024.107053. URL: https://www.sciencedirect.com/science/article/pii/S0584854724001976.

[19] Thomas N. Woods et al. "Scattered-light properties of diffraction gratings". In: *Appl. Opt.* 33.19 (July 1994), pp. 4273–4285. DOI: 10.1364/AO.33.004273. URL: https://opg.optica.org/ao/abstract.cfm?URI=ao-33-19-4273.

[20] Yuming Wang et al. "Optical Design for Aberration Correction of Ultra-Wide Spectral Range Echelle Spectrometer". In: *Photonics* 9.11 (2022). ISSN: 2304-6732. DOI: 10.3390/photonics9110841. URL: https://www.mdpi.com/2304-6732/9/11/841.

[21] Yajun Pang et al. "Compact high-resolution spectrometer using two plane gratings with triple dispersion". In: *Opt. Express* 26.5 (Mar. 2018), pp. 6382–6391. DOI: 10.1364/OE.26.006382. URL: https://opg.optica.org/oe/abstract.cfm?URI=oe-26-5-6382.

[22] Hyung-Su Chon et al. *The dependence of transverse and longitudinal resolutions on incident Gaussian beam widths in the illumination part of optical scanning microscopy*. 2006. arXiv: physics/0411222 [physics.optics]. URL: https://arxiv.org/abs/physics/0411222.

[23] Thorlabs. *GR25-0610, 1 μm Blaze Wavelength Reflective Diffraction Gratings Efficiency Curve*. Accessed: 2025-10-27. 2025. URL: https://www.thorlabs.com/images/tabImages/1000_600_Ruled_Grating_Efficiency_Graph_780-2.gif.

[24] Sima Bahrani, Mohsen Razavi, and Jawad A. Salehi. "Wavelength Assignment in Hybrid Quantum-Classical Networks". In: *Scientific Reports* 8.1 (Feb. 2018), p. 3456. ISSN: 2045-2322. DOI: 10.1038/s41598-018-21418-6. URL: https://doi.org/10.1038/s41598-018-21418-6.

[25] Jian Li and Mingjiang Zhang. "Physics and applications of Raman distributed optical fiber sensing". In: *Light: Science & Applications* 11.1 (May 2022), p. 128. ISSN: 2047-7538. DOI: 10.1038/s41377-022-00811-x. URL: https://doi.org/10.1038/s41377-022-00811-x.

[26] Qi Wu et al. "Integration of quantum key distribution and high-throughput classical communications in field-deployed multi-core fibers". In: *Light: Science & Applications* 14.1 (Aug. 2025), p. 274. ISSN: 2047-7538. DOI: 10.1038/s41377-025-01982-z. URL: https://doi.org/10.1038/s41377-025-01982-z.

[27] L. A. Ribeiro et al. "Asymmetries of Spontaneous Raman Scattering in Optical Fibers for the Forward-Backward Directions". In: *Advanced Photonics & Renewable Energy*. Optica Publishing Group, 2010, JThA20. DOI: 10.1364/SENSORS.2010.JThA20. URL: https://opg.optica.org/abstract.cfm?URI=Sensors-2010-JThA20.